NASA/TP—2003–212284

Pulse Detonation Rocket Magnetohydrodynamic Power Experiment

R.J. Litchford, J.E. Jones, C.C. Dobson, and J.W. Cole
Marshall Space Flight Center, Marshall Space Flight Center, Alabama

B.R. Thompson
TMET, Winchester, Tennessee

D.H. Plemmons
Plemmons Consulting, Lynchburg, Tennessee

M.W. Turner
The University of Alabama in Huntsville, Huntsville, Alabama

February 2003

The NASA STI Program Office…in Profile

Since its founding, NASA has been dedicated to the advancement of aeronautics and space science. The NASA Scientific and Technical Information (STI) Program Office plays a key part in helping NASA maintain this important role.

The NASA STI Program Office is operated by Langley Research Center, the lead center for NASA's scientific and technical information. The NASA STI Program Office provides access to the NASA STI Database, the largest collection of aeronautical and space science STI in the world. The Program Office is also NASA's institutional mechanism for disseminating the results of its research and development activities. These results are published by NASA in the NASA STI Report Series, which includes the following report types:

- TECHNICAL PUBLICATION. Reports of completed research or a major significant phase of research that present the results of NASA programs and include extensive data or theoretical analysis. Includes compilations of significant scientific and technical data and information deemed to be of continuing reference value. NASA's counterpart of peer-reviewed formal professional papers but has less stringent limitations on manuscript length and extent of graphic presentations.

- TECHNICAL MEMORANDUM. Scientific and technical findings that are preliminary or of specialized interest, e.g., quick release reports, working papers, and bibliographies that contain minimal annotation. Does not contain extensive analysis.

- CONTRACTOR REPORT. Scientific and technical findings by NASA-sponsored contractors and grantees.

- CONFERENCE PUBLICATION. Collected papers from scientific and technical conferences, symposia, seminars, or other meetings sponsored or cosponsored by NASA.

- SPECIAL PUBLICATION. Scientific, technical, or historical information from NASA programs, projects, and mission, often concerned with subjects having substantial public interest.

- TECHNICAL TRANSLATION. English-language translations of foreign scientific and technical material pertinent to NASA's mission.

Specialized services that complement the STI Program Office's diverse offerings include creating custom thesauri, building customized databases, organizing and publishing research results…even providing videos.

For more information about the NASA STI Program Office, see the following:

- Access the NASA STI Program Home Page at ***http://www.sti.nasa.gov***

- E-mail your question via the Internet to help@sti.nasa.gov

- Fax your question to the NASA Access Help Desk at (301) 621–0134

- Telephone the NASA Access Help Desk at (301) 621–0390

- Write to:
  NASA Access Help Desk
  NASA Center for AeroSpace Information
  7121 Standard Drive
  Hanover, MD 21076–1320
  (301)621–0390

NASA/TP—2003–212284

Pulse Detonation Rocket Magnetohydrodynamic Power Experiment

R.J. Litchford, J.E. Jones, C.C. Dobson, and J.W. Cole
Marshall Space Flight Center, Marshall Space Flight Center, Alabama

B.R. Thompson
TMET, Winchester, Tennessee

D.H. Plemmons
Plemmons Consulting, Lynchburg, Tennessee

M.W. Turner
The University of Alabama in Huntsville, Huntsville, Alabama

National Aeronautics and
Space Administration

Marshall Space Flight Center • MSFC, Alabama 35812

February 2003

Acknowledgments

This work was sponsored by the Space Transportation Research Project Office, Advanced Space Transportation Program, Marshall Space Flight Center. The NASA Principal Investigator was Ron J. Litchford, Project Scientist, Space Transportation Research Project Office, TD15/ASTP.

TRADEMARKS

Trade names and trademarks are used in this report for identification only. This usage does not constitute an official endorsement, either expressed or implied, by the National Aeronautics and Space Administration.

Available from:

NASA Center for AeroSpace Information
7121 Standard Drive
Hanover, MD 21076–1320
(301) 621–0390

National Technical Information Service
5285 Port Royal Road
Springfield, VA 22161
(703) 487–4650

TABLE OF CONTENTS

1. INTRODUCTION 1

2. EXPERIMENTAL APPARATUS 3

2.1 Integrated Injector/Initiator Assembly 3
2.2 Primary Engine Tube 3
2.3 Converging-Diverging Nozzle 4
2.4 Magnetohydrodynamic Generator 4
2.5 Microprocessor-Based Engine Control System 5

3. SHAKEDOWN TESTING 6

3.1 Detonation Characteristics 6
3.2 Installed Thrust Characteristics 7

4. ENGINE EXHAUST CHARACTERIZATION 9

4.1 Emission Spectroscopy 9
4.2 Microwave Interferometer Interrogation 10

5. MAGNETOHYDRODYNAMIC TESTING 13

6. CONCLUSIONS 15

REFERENCES 16

LIST OF FIGURES

1. Schematic of the NASA MSFC PDRE–G–2 research engine. The major flow path components are: (1) Integrated injector/initiator assembly, (2) primary tube, (3) converging-diverging nozzle section, and (4) segmented Faraday channel (0.6-T permanent magnet assembly not shown). The system exhausts into the open atmosphere 19

2. Cross-sectional drawing of the integrated injector/initiator assembly 20

3. Schelkin spiral insert for primary detonation tube 21

4. Schematic of aluminum nozzle assembly 22

5. Exploded schematic of segmented Faraday channel with 24 active electrode pairs 23

6. Schematic of fully assembled PDRE–G–2 research engine on the thrust stand with nozzle and MHD generator attached 24

7. Axial pressure profiles without nozzle as measured at ports 1 through 8 25

8. Axial pressure profiles with nozzle as measured at ports 1 through 8 26

9. Combustion wave velocity distribution 27

10. Ideal tube head pressure profile for a nozzleless straight-tube pulse detonation engine with head-end ignition 28

11. Time-resolved tube head pressure and installed thrust profiles without nozzle 29

12. Time-resolved tube head pressure and installed thrust profiles with nozzle 30

13. Summary of emission spectroscopy survey at engine nozzle exit 31

14. Synthetic spectra of the OH band head at 306 nm as generated by the NASA NEQAIR radiation code for equilibrium temperatures of 4,000, 3,500, 3,000, and 2,500 K. Assumes an electronic temperature of 10,000 K 32

LIST OF FIGURES (Continued)

15. Schematic of polychromatic quadrature microwave interferometer 33

16. Summary of microwave interferometer interrogation of the PDRE–G–2 engine exhaust at the nozzle exit plane: (a) 70-GHz calibration, attenuated calibration, and data; (b) 90-GHz calibration, attenuated calibration, and data; (c) 110-GHz calibration, attenuated calibration, and data; (d) raw signal from 70-GHz channel; (e) attenuation factor for all three channels; and (f) electron number density as measured for all three interrogation frequencies 34

17. Summary of MHD testing using the PDRE–G–2 research engine: (a) 1-MΩ load and implied effective velocity, (b) 1-kΩ load, (c) 100-Ω load, and (d) 3-Ω load 35

LIST OF ACRONYMS AND SYMBOLS

CCD	charged coupled device
CFD	computational fluid dynamics
C–J	Chapman-Jouget (detonation condition)
Cs	cesium
H	hydrogen
LVDT	linear variable displacement transducer
MHD	magnetohydrodynamic
MSFC	Marshall Space Flight Center
NEQAIR	nonequilibrium air
O	oxygen
TTL	transistor-transistor logic

NOMENCLATURE

A	cross-sectional area
B	magnetic field strength (induction)
c	speed of light
D	dark signal
d	pathlength
E	electric field
E_H	electric field of the reflected scene beam
E_R	electric field of the reference beam
E_S	electric field of the primary scene beam
h	channel height
i	current
K	calibration constant
L	length
m_e	mass of electron
n	number density
n_c	critical number density
q_e	electron charge
R	resistance
R_d	resistance associated with near-electrode voltage drop
R_i	internal resistance
R_L	load resistance
R_p	core plasma resistance
S	signal
S'	quadrature signal
$S(\Delta x)$	calibration data for signal detector
$S'(\Delta x)$	calibration data for quadrature signal detector
u	velocity
V	voltage

NOMENCLATURE (Continued)

x	distance
β	initial phase shift due to reflection
γ	detector responsivity
γ'	quadrature detector responsivity
Δ	dimensionless effective voltage drop
Δx	physical pathlength
ε_0	permittivity of free space
θ_0	quadrature phase shift
λ	wavelength
φ	phase shift through measurement volume
φ_0	initial phase angle between reference beam and scene beam at the input detector
ω	microwave frequency

TECHNICAL PUBLICATION

PULSE DETONATION ROCKET MAGNETOHYDRODYNAMIC POWER EXPERIMENT

1. INTRODUCTION

It is widely recognized that pulse detonation engine architectures, as applied to aerospace propulsion applications, may yield substantial improvements in performance, design simplicity, and cost. There is also a growing recognition that variant architectures for aerospace electrical power generation, particularly burst-mode power, may also yield similar improvements.

The amount of research currently being generated with respect to potential propulsion applications is truly immense. The reader is referred to the recent review paper of Kailasanath for an excellent overview of the subject, including thorough discussion of the potential performance advantages, ongoing domestic and international research programs, major scientific advances, and outstanding research issues.[1] The amount of research on electrical power generation, on the other hand, has been extremely limited.

This is somewhat surprising from a systems point of view, since a pulse detonation engine may require a significant amount of base operational power, both for ignition and propellant pumping, as well as auxiliary power for onboard electrical systems. Furthermore, traditional pulse detonation engine architectures do not produce useable shaft power, and some other form of energy conversion is required. It is conceivable that energy could be extracted from the mechanical thrust, using piezoelectric devices for instance, but others have suggested that magnetohydrodynamic (MHD) power generation may prove more effective, especially for meeting burst power needs.[2–7]

Previous research using a small-scale oxy-acetylene device (2.54-cm × 2.0-cm MHD channel) with low applied magnetic field (0.6 T) has demonstrated some difficulties with this approach.[2,4–6] The two major problems encountered in those experiments were (1) high near-electrode voltage drop (≈60 percent of induced potential) and (2) lower than expected MHD interaction. The dominance of the boundary layer voltage drop was mainly due to the large surface-to-volume ratio of the device, which accentuated the surface effect losses, and to cold electrode surfaces (single-shot apparatus). The lower than expected MHD interaction was mainly due to a low effective value for the electrical conductivity (≈6 S/m) and low local flow velocity (≈660 m/s) at peak electrical conductivity. Related CFD calculations by Cambier suggest that the latter effect may be the result of kinetic delays which cause the ionization wave to lag the detonation front by a significant time increment.[3,7]

Because the previous experiments were conducted in a straight flow path, such an effect would be extremely detrimental with regard to performance. One method for circumventing this kinetic delay phenomena is to geometrically focus the detonation wave, as suggested by Cambier.[7] In practice, this can

be accomplished by focusing the detonation wave through a converging nozzle section followed by expansion to high velocity in a diverging nozzle section. If the free electron concentration can be frozen in during the expansion process, the flow should be optimally conditioned for driving an attached MHD generator.

Following this line of thought, a new experimental apparatus was developed which provides a suitable framework for investigating this concept. This device is a straightforward extension of a low-cost, gas-fed, pulse detonation research engine (model PDRE–G–1) which was recently developed and tested at NASA Marshall Space Flight Center (MSFC).[8]

The new pulse detonation driver for this experiment, designated as model PDRE–G–2, is similar in most respects to model PDRE–G–1 except that it is based on a square rather than a round cross section. This was done to make physical integration with an MHD channel more amenable. This Technical Paper describes the development of the thermal driver (engine model PDRE–G–2) and MHD generator flow path and presents results from the initial set of experiments.

2. EXPERIMENTAL APPARATUS

The mechanical design of the NASA MSFC PDRE–G–2 research engine was derived directly from the design of the predecessor PDRE–G–1 engine, which was fully reported in a previous publication.[8] Both are simple, flexible, and inexpensive research apparatus under no pretense of being evolutionary steps toward a practical production engine. As such, they are designed as heat sink devices and are limited to burst mode operation of a few seconds duration, which is adequate for most research purposes.

The fully assembled PDRE–G–2 flow path components are shown schematically in figure 1. The major components are the integrated injector/initiator, primary detonation tube, converging-diverging nozzle, and segmented Faraday channel. Use was made of standard off-the-shelf industrial or automotive components wherever possible. Components requiring custom fabrication were designed to be as simple and inexpensive as possible with little or no consideration given to long-term survivability or aesthetic notions. The only special design provisions were those associated with ensuring diagnostic access. The existing propellant storage and delivery system and rigidized test stand, as originally developed for the PDRE–G–1 research engine, were directly usable without modification. The existing microprocessor-based engine control system was also directly applicable.

2.1 Integrated Injector/Initiator Assembly

Gaseous hydrogen (H) and oxygen (O) enter the engine through a coaxial injector attached to the end of the detonation initiator so that the propellants are thoroughly mixed before they enter the primary tube. Two special design, fast-response solenoid valves (<1 ms opening and closing) acquired from ValveTech Inc. (PN VTI 15060–2) were used to intermittently sequence propellant flow through the injector.

Fundamentally, the initiator is just a 15.25-cm-long, 1.1-cm-diameter circular hole with an automotive spark plug inserted near the injector, as shown in figure 2. A Schelkin spiral formed from 1/40-in-diameter wire coiled into a 1/4-in pitch helix is also inserted in the initiator to promote turbulent mixing and ensure rapid deflagration-to-detonation transition. The reliable performance of this design was previously demonstrated.[8] The initiator is inserted to a depth of 2 cm through the head-end flange of the primary tube with the intent of propagating the detonation wave into the primary tube and igniting the main propellant charge.

2.2 Primary Engine Tube

The basis for the primary detonation tube was a 90-cm-long section of standard 2-in × 2-in square stainless steel tubing. The 0.12-in-thick walls yield a 4.5-cm × 4.5-cm internal cross section. This approach was inexpensive and expedient and provided sufficient design margin for heat sink mode operation. Flanges were welded on each end of the tube to accept the injector/initiator assembly and the nozzle section. The head-end blind flange also included a wall pressure tap.

Pressure sensor ports were located at 10-cm intervals along the tube, and two diametrically opposing spark plug ports were located 5 cm downstream from the head-end flange. A Schelkin spiral insert was created by coiling 1/16-in-diameter wire into a 1/4-in-pitch shape, conforming to the square internal cross section. The resulting spiral was then inserted over one-third the length of the primary tube, as shown in figure 3.

In order to enhance ionization and modify the electrical conductivity of the engine exhaust, it was necessary to inject an alkali metal seed material prior to ignition during each engine cycle. Based on previous experience, it was decided to inject a 30-percent solution (by mass) of cesium (Cs)-hydroxide in a methanol carrier as an atomized spray. An electrically activated atomizing fuel injector for an automotive engine was adapted for use and mounted in a boss located 20 cm upstream from the nozzle entrance. The injector was then calibrated as a function of reservoir pressure and actuation time to deliver ≈1 percent seed concentration in the propellant. An extra digital control signal was also added to the microprocessor-based engine control system to provide properly timed actuation of the seed injection process.

2.3 Converging-Diverging Nozzle

Geometrical focusing of the detonation wave and subsequent expansion to high velocity was accomplished with a converging-diverging nozzle. The hope was that the free electron concentration would be frozen-in during the expansion process, such that a highly ionized condition could be maintained even as the gas cooled during the expansion. Unfortunately, the allowable degree of expansion was limited by the air gap (3.5 cm) of the available permanent magnet assembly.

Based on this limitation, it was decided to design the nozzle with an area contraction ratio of A^*/A_c=1/10 which, given the fixed primary tube dimensions, yields an area expansion ratio of A_e/A^*=3 with a 2.54-cm × 2.54-cm internal cross section at the nozzle exit. This dimension was compatible with the constraining magnet air gap with the remaining spatial envelope large enough to accommodate a practical channel design. The entire nozzle section is 11.5 cm long.

The nozzle was machined from four aluminum pieces that mated together to form a three-dimensional converging-diverging flow path, as shown in figure 4. The contraction and expansion were machined with fixed angles on all four walls in order to hold an aspect ratio of unity through the nozzle. This assembly was pinned together and designed for easy attachment or removal using four bolts.

2.4 Magnetohydrodynamic Generator

A segmented Faraday channel, shown schematically in figure 5, was designed and fabricated to mate with the nozzle assembly and fit through the available permanent magnet assembly. The internal flow passage was 2.54 cm square. The channel has 24 copper alloy electrode pairs that are 1.5 cm wide and insulated from each other by high-temperature ceramic tape. The sidewalls are formed from two G–10 phenolic plates which have been machined to accept the electrodes. The sidewalls are bolted together, clamping the electrodes in place, and the whole channel is connected to the nozzle using four tie rods. Each electrode has an individual lead wire that is routed to a patch panel for convenient alteration of the load configuration.

2.5 Microprocessor-Based Engine Control System

Precise control over valve and ignition timing was provided by a microprocessor-based engine control system, which was previously developed and demonstrated on the PDRE–G–1 research engine.[8] The TTL control signals are generated by an eight-channel, 32-bit counter/timer module with software control under a customized program written in National Instruments Corporation's LabVIEW™ graphical programming language. This program permits precise adjustment of the duty cycle and phasing of each control signal.

The control signals are converted to light pulses by TTL optical transmitters and fiber optically coupled to TTL optical receivers. For valve actuation and seed injector control, the TTL optical receivers are coupled to solid state relay switches, which control power to the various valves. For engine ignition, the TTL optical transmitter is fed to a transistor switch, which activates an electronic automotive ignition system. In this case, three independent spark ignition systems are utilized.

3. SHAKEDOWN TESTING

Upon final assembly of the experimental apparatus, a number of shakedown tests were conducted to validate functionality of the device and obtain basic performance data. All of these tests were conducted with near-stoichiometric H/O propellant mixtures. A schematic of the fully assembled PDRE–G–2 research engine with the nozzle and MHD generator attached is shown installed on the test stand in figure 6.

The primary tube was outfitted with dynamic pressure transducers at the indicated port locations as a means of monitoring combustion wave characteristics. Also note that the engine was equipped with a thrust transmission structure and a dynamic load cell for the purpose of making time-resolved thrust measurements with and without the nozzle attachment.

Although the engine would successfully fire using the initiator as the only ignition source, two diametrically opposed spark plugs were installed in the primary tube to provide redundant ignition sources and thereby reduce the chance for misfire. With only two valves and limited propellant supply pressure, the engine operating frequency was limited to no more than 4 Hz.

3.1 Detonation Characteristics

The first test firings were conducted with the nozzle removed and the tube open to the atmosphere. Measured pressure waveforms acquired at the primary tube sensor ports are shown in figure 7. Each waveform corresponds to one of the eight sensor ports in the tube. It is clear from the resulting waveforms that the Schelkin spiral is successfully aiding in the rapid development of a detonation wave near the head-end of the primary tube. The waveform shapes exhibit the classic characteristics of combustion detonation waves. The steep-fronted leading edge associated with the shock sharply rises to a pressure consistent with the expected value for a C–J detonation and then slowly decays to a postcombustion value in the range of 5 to 10 atm, as anticipated for H/O propellants. The indicated combustion wave velocity (≈3 km/s) is also consistent with the C–J value for these propellants at near stoichiometric mixture ratios.

A second set of test firings were conducted with the nozzle attached, resulting in the primary tube pressure waveforms shown in figure 8. Again, the detonation wave exhibits classical behavior; however, the peak pressure is slightly decreased from the nozzleless case and the wave speed is slightly repressed (≈2.5 km/s). This result seems to indicate a significant shift in stoichiometry. It is the authors' belief that the presence of the converging-diverging nozzle alters the fluid dynamics of the propellant injection process within the primary tube, but no attempt was made to tune and optimize the injection conditions, since the detonation characteristics were sufficiently close to optimal.

An important feature to note in these pressure waveforms is the emergence of a weak reflected pressure wave from the convergent nozzle entrance (see the profile for the last sensor port). This behavior was anticipated and could provide favorable heating of the gas near the nozzle throat if sufficiently strong. In this case, it is observed that the pressure wave rapidly assumes a bulge profile as the gas rushes back toward the tube head.

Using the previously obtained pressure waveforms, it was possible to construct the combustion wave velocity distributions within the primary tube. The results for both cases are summarized in figure 9. Here, it is observed that the combustion wave accelerates to detonation speed after traveling about one-third the length of the primary tube. Interestingly, this corresponds to the length of the Schelkin spiral insert. From that point, the detonation wave tends to propagate to the end of the tube with a very minor decrease in velocity. Both cases exhibit the same general trend, except the case with the nozzle attached is shifted to slightly lower velocities, as previously noted.

3.2 Installed Thrust Characteristics

The installed engine thrust characteristics were also of particular interest, and the availability of a fast response dynamic load cell provided an opportunity to acquire time-resolved thrust profiles. This technique had been successfully implemented during testing of the PDRE–G–1 research engine,[8] and an identical technique was implemented here.

As noted during previous testing with the PDRE–G–1 research engine, the actual thrust profile depends on the tube fill conditions. If the tube is completely filled with propellant, the detonation wave propagates the entire length of the tube and fills it with combustion gases which are then expelled during the subsequent blowdown process. If the tube is only partially filled, however, some quantity of air must be pushed out by the trapped combustion gases. Maximum impulse occurs for the filled tube condition, but, interestingly, maximum specific impulse can occur when the tube is only partially filled. This is a significant effect deserving of exhaustive study. Current testing with the PDRE–G–2 research engine, however, was limited to filled tube conditions, since the focus of this investigation was MHD power generation.

The term “installed thrust” is used because the engine and thrust transmission structure effectively behave as a spring-damper system. As such, the measured thrust profile depends on the dynamic response of the installed engine structure. Therefore, the installed engine thrust does not necessarily correspond with the fluid dynamic force profile acting on the engine surfaces.

As shown in figure 10, the ideal tube head pressure profile for a nozzleless straight-tube engine assumes a constant value until the left running rarefaction wave, generated when the detonation exits the tube, returns to the tube head surface. The remaining portion of the ideal pressure profile can then be approximated as an exponential decay as gases are expelled during the subsequent blowdown process.

The actual tube head pressure profile and installed thrust profiles obtained with the nozzleless PDRE–G–2 engine are shown in figure 11. Here, we observe a sharp spike corresponding to initiation of the cycle followed by a pressure dip, a short region of constant pressure (≈6 atm), and an exponential decay. Except for the dip, this profile is remarkably similar to the idealized tube head pressure profile. The pressure dip remains an unresolved fluid dynamic phenomenon at this time, although it is believed to result from the interaction of the emerging initiator jet with the combustion fronts originating from the redundant spark plugs. The installed thrust profile does not follow the pressure profile, which would require perfect structural response, but rather exhibits a basic bulge shape (≈350 lbf peak).

The measured tube head pressure and installed thrust profiles with the nozzle attached are shown in figure 12. In this case, the tube head pressure continues to oscillate as the pressure internally reflects within

the primary tube. As a result, the installed thrust profile also oscillates, and, because high-pressure regions periodically form near the nozzle entrance, the installed thrust actually becomes negative during portions of the engine cycle. Although the installed thrust profiles have yet to be integrated, it appears that the total impulse with the nozzle will be considerably less than that for a nozzleless engine. Therefore, it is expected that integrating a nozzled MHD generator with a pulse detonation engine will lead to some propulsive performance loss. For many applications where power generation is more important than propulsive efficiency, this may not necessarily be detrimental.

4. ENGINE EXHAUST CHARACTERIZATION

Prior to conducting the MHD generator tests, an attempt was made to characterize the engine exhaust at the exit plane of the nozzle. Because MHD performance is strongly dependent on the level of electrical conductivity, it was desirable to have some quantitative measure of the plasma conditions at the entrance to the generator. The diagnostics included basic emission spectroscopy and interrogation of the plasma using a newly developed polychromatic microwave interferometer.

4.1 Emission Spectroscopy

Emission from the seeded exhaust plume was examined using a gated PIMAX 512×512 intensified charged coupled device (CCD) detector mated to an ISA Jobin YVON–Spex 1/4-m spectrometer with a 1,200-groove/nm grating. The results of the emission spectroscopy survey over the optical region are summarized in figure 13.

The only prominent features in the spectra are numerous atomic transition lines for Cs, the OH(A–X) band head at 306 nm, and the sodium D lines. These results indicated that relatively good combustion efficiency was obtained and that there were no major contaminants in the plume.

An attempt was made to deduce temperature by fitting the experimental OH band with a synthetic spectra generated with the NASA nonequilibrium air (NEQAIR) radiation code.[9] This code is capable of generating the emission and absorption spectra for atomic and diatomic species and computing the transport of optical radiation through a nonuniform gas mixture to a surface along a specified line of sight.

The atomic and rotational lines and vibrational bands for each molecule as well as bound-free and free-free continua caused by the interaction of free electrons with neutral and ionized atoms are used to compute the total optical spectrum in a discrete layer of gas in which the species concentrations and temperatures are assumed to be constant. This result is then used as the incident spectrum for the adjacent discrete gas layer, and the process is repeated layer by layer along the line of sight until the desired detection surface is reached.

The NEQAIR code, as adapted for utilization on a PC platform, is currently being used to support internal research at MSFC. In the present case, the species concentrations were estimated from thermodynamic equilibrium calculations and our PC version of the NEQAIR code was used to obtain the synthetic spectra, assuming an electronic temperature of 10,000 K (since the OH emission is most likely associated with chemiluminescence). The resulting synthetic spectra are shown in figure 14, assuming equilibrium temperatures of 4,000, 3,500, 3,000, and 2,500 K.

Clearly, the overall profile of the synthetic spectra does not change much over this temperature range, and much higher fidelity data are required to defend any sort of fit. In order to deduce temperature with some degree of confidence, it is necessary to resolve the rotational structure in the experimental spectra and the NEQAIR spectra to the same degree of fidelity. This will require higher resolution

measurements than obtained in the current study and accurate evaluation of line strengths, line broadening, and absorption. Nevertheless, comparison of the spectra at the current level of fidelity gives some indication that the temperature at the nozzle exit is in the neighborhood of 3,000 K.

4.2 Microwave Interferometer Interrogation

A newly developed polychromatic quadrature microwave interferometer was used to interrogate the plasma jet at the exit plane of the PDRE–G–2 engine nozzle. This device, shown in the schematic of figure 15, simultaneously transmits and receives three discrete beam frequencies (70, 90, and 110 GHz) and can be operated in reflectometer mode. Here, the three scene beams were spatially superimposed and focused with 1/2-m focal length Gaussian optics such that the 1.25-cm focal spot was directly on the centerline of the nozzle axis. The reference beams were routed through low-loss coaxial cables at lower frequencies and then multiplied before being sent to the quadrature mixers.

The mixer outputs were then measured at each of two detectors: (1) The input detector, where portions of the reference and scene beams are combined directly, and (2) the quadrature detector, where the scene beam portion is quadrature shifted before combination. The data reduction analysis assumes that there is no crosstalk between beams of different frequencies; thus, each frequency is treated independently.

The data from the interferometer shows multiple reflections occurring between the receiving and transmitting horns. For this analysis, only the first reflected signal was considered. Thus, only the portion of the scene beam that passes a single time through the measurement volume, and the portion that is transmitted through the measurement volume three times, are analyzed. The following expressions have been derived for the interferometer signals for this case.[10] The signal at the input detector is given by

$$\frac{S-D}{\gamma c \varepsilon_0} = E_R^2 + E_S^2 + E_H^2 + 2\left[E_R E_S \cos(\varphi+\varphi_0) + E_R E_H \cos(3\varphi+\varphi_0+\beta) + E_S E_H \cos(2\varphi+\beta)\right] \quad (1)$$

and the signal at the quadrature detector is given by

$$\frac{S'-D'}{\gamma' c \varepsilon_0} = E_R'^2 + E_S'^2 + E_H'^2 + 2\left[E_R' E_S' \cos(\varphi+\varphi_0+\theta_0) + E_R' E_H' \cos(3\varphi+\varphi_0+\theta_0+\beta) + E_S E_H \cos(2\varphi+\beta)\right] , \quad (2)$$

where E_R, E_S, and E_H are the electric fields of the reference beam, the primary scene beam, and the reflected scene beam, respectively; D is the dark signal; γ is the detector responsivity; φ_0 is the initial phase angle between the reference beam and (primary) scene beam at the input detector; β is the initial phase shift due to reflection; θ_0 is the quadrature phase shift, which is ideally 90°; and φ is the phase shift through the measurement volume.

The quantity the authors are interested in is φ, which is related to the electron density along the line of sight by

$$\varphi = -\frac{\omega}{c}\left[d - \int_0^d \left[1-\frac{n(x)}{n_c}\right]^{1/2} dx\right] = -\frac{2\pi}{\lambda}\int_0^d 1-\left[1-\frac{n(x)}{n_c}\right]^{1/2} dx \ , \quad (3)$$

where ω is the microwave frequency, λ is the wavelength, $n_c = \omega^2 \varepsilon_0 m_e / q_e^2$ is the critical density, $n(x)$ is the density profile, and d is the pathlength.[11] When the electron density is much less than the critical density, equation (3) can be approximated by

$$\varphi \approx -\frac{\pi}{\lambda} \int_0^d \frac{n(x)}{n_c} dx \tag{4}$$

from which the chord-averaged electron density can readily be obtained by assuming a constant value for the electron density.

In order to determine φ, the physical fields are redefined as relative fields, $E_R \rightarrow \sqrt{\gamma c \varepsilon_0} E_R$, and so on. Calibration data $S(\Delta x)$ and $S'(\Delta x)$ are obtained by varying the physical pathlength, Δx, between the transmit and receive horns and recording the displacement with a linear variable displacement transducer (LVDT). With this data, the calibration parameters E_R, E_S, E_H, E'_R, E'_S, E'_H, D, D', φ_0, θ_0, and β can be determined by fitting to equations (1) and (2). In addition, a calibration constant for the LVDT was obtained with the fitting routine by noting that $\varphi = K\, V_{LVDT}$ and fitting for $K \equiv (2\pi/\lambda)(dx/dV_{LVDT})$.

During an engine pulse, the microwave signal from the scene beam(s) is attenuated and phase shifted. Fortunately, in the quadrature setup, equations (1) and (2) can be used with the input and quadrature signals to solve for the phase shift and the change in amplitude of E_S and E_H along with their primed counterparts. To do this, it is assumed that the attenuation is due only to the exhaust plume and that the input and quadrature signals are attenuated by the same amount. Also, the attenuation factor is cubed for E_H, because it passes through the plume three times. This allows us to solve for two unknowns, the phase shift and an attenuation factor, assuming the values of the remaining calibration parameters remain constant. This procedure contains a degree of uncertainty in that the absolute values of the dark signals and electric fields can only be uniquely determined if the signals contain no noise. This limitation especially affects data with high attenuation.

The results from the microwave interferometer interrogation are summarized in figure 16 where all signals have been acquired at 50 kHz using a 12-bit digitizer. The reduced data for the 70-, 90-, and 110-GHz channels are shown in figures 16(a)–16(c), respectively. Here, the dashed curve is the calibration data with no attenuation of the beam; the solid curve is the curve fit to the calibration data near maximum phase shift when the scene beam and reflected beam are highly attenuated; and the circles are the time-resolved data captured during a single engine pulse. The calibration curve is actually fitted for each data point but these results are not shown for clarity. Note that rotation of the data points about the calibration ellipse represents the instantaneous phase shift of the scene beam during its passage through the engine exhaust. Raw signals for the 70-GHz channel are shown in figure 16(d) for illustrative purposes. The time-resolved attenuation factor is plotted for all three channels in figure 16(e). The electron number density is shown in figure 16(f) as measured at all three interrogation frequencies.

The passage of the detonation wave is marked by a sharp rise in the electron number density. In fact, the phase shift from the interferometer goes from the initial phase angle to the maximum phase shift within the first 40 μs of the pulse. The strongest portion of the detonation wave passes in the first 0.5 ms,

but the blowdown period lasts for more than 2 ms. The highest attenuation is coincident with the maximum phase shift or electron density, placing the highest uncertainty in the electron density measurement at the peak of the detonation pulse. This uncertainty is evident in the larger spread in electron density between the different frequencies at the peaks.

It is interesting to note the differences in the predictive behavior of all three frequencies, which ideally would yield identical electron densities. If the peak associated with detonation wave passage is ignored, for example, the 70-GHz signal is attenuated the most and the 110-GHz signal the least. Furthermore, the 70-GHz channel yields the highest electron density, while the 110-GHz channel measures the lowest electron density. These discrepancies are relatively small, however, and all channels yield measured chord-averaged electron number densities on the order of 10^{12} cm^{-3} with a high degree of confidence.

It is not clear at this time why such drastic attenuation of the scene beam is observed during passage of the detonation wave. Nevertheless, the data are conclusive in this respect, and the authors must conclude that some physical phenomena occurs behind the detonation shock wave giving rise to attenuation (absorption and/or scattering) of impinging microwave beams. Further investigation will be necessary to resolve this issue.

5. MAGNETOHYDRODYNAMIC TESTING

The preceding engine exhaust characterization tests indicated that the ionization conditions at the entrance to the generator should be sufficient to evoke MHD interaction. Thus, the 24-electrode segmented Faraday channel was attached to the nozzle, and each electrode pair was individually loaded. The engine was then operated with seed injection, under the same conditions used for the exhaust characterization tests, while capturing the time-resolved terminal voltages of the generator. The results from these MHD tests are summarized in figure 17 for load impedances of 10^6, 10^3, 10^2, and 3 Ω. Note that all electrode pairs were identically loaded during each test. The three-dimensional plots of figure 17 show the terminal voltage distribution along the channel electrodes as a function of time.

For all practical purposes, the test with 1-MΩ loading corresponds to open circuit conditions, and it was possible to scale the resulting terminal voltage to obtain a measure of the effective velocity in the channel using the fact that $V_L \approx \varepsilon = uBh$ as the current approaches zero. The result of this scaling is shown in figure 17(a) where peak velocities between 1,400 and 1,500 m/s are observed. This is, admittedly, a crude measurement of channel velocity, since the boundary layer voltage drops conceal the true potential across the core, but it does provide a reasonably effective value for estimation purposes.

The peak terminal voltage for the 1-MΩ loaded case fluctuates in the range of 20 to 25 V. As the load impedance is reduced, the terminal voltage should decrease as more current is applied to the load and more power is extracted. In our case, however, the observed generator terminal voltage drops precipitously as the load impedance is only slightly reduced. For the 10-kΩ load, for example, the peak output is down to ≈10 V. At 100 Ω, the peak output fluctuates around 2 V; and at 3 Ω, the output is in the noise.

The root cause of this poor performance is that well-recognized old difficulty that has plagued MHD engineering since its inception—near-electrode voltage drop. This problem is the major reason that MHD device performance tends to improve dramatically with increasing scale. That is, as the surface-to-volume ratio becomes small, the core processes can become dominant. Therefore, it is not really surprising that our small-scale device with limited channel height and limited applied magnetic field strength suffers immense performance penalties.

The magnitude of the problem is evident from consideration of Kirchoff's voltage law as applied to the channel:

$$\varepsilon = uBh = iR_L + iR_\mathrm{i} \quad , \tag{5}$$

where i is the current, R_L is the load resistance, and R_i is the internal resistance of the generator including boundary layer potential losses. Substituting $i = V_L/R_L$ into equation (5), it is possible to derive a simple expression for the internal generator resistance in terms of the known load impedance and the measured terminal voltage:

$$R_i = \left(\frac{uBh}{V_L} - 1 \right) R_L \quad . \tag{6}$$

Using representative values from these experiments, the authors deduce that $R_i = R_p + R_d \approx 10^3\ \Omega$, where R_p is the core plasma resistance and R_d is the resistance associated with the near-electrode voltage drop. Furthermore, diagnostic investigations imply that the core electrical conductivity is relatively high, such that $R_p << R_d$. Thus, it may be concluded that $\Delta = V_d/uBh \approx 1$ in this experiment.

The performance can be improved, of course, by increasing the induced potential. This requires increasing channel velocity, applied magnetic field, and/or channel height in some combination that results in a major increase in ε. In the present experiment, all of these parameters were constrained by the available magnet. A refurbished 2-T electromagnet with an air gap of 4 in is being brought online at MSFC and should alleviate this limitation with regard to future testing.

With a large bore magnet, it is also clear that a much larger nozzle expansion ratio could be implemented. This would have allowed us to attain a considerably high channel velocity without suffering a major sacrifice in electrical conductivity. It is even conceivable that the achievable expansion might be great enough to obtain a high Hall parameter, thereby permitting exploration of Hall-configured generators for this application.

Another possibility, originally suggested by Cambier, is to investigate inductive load coupling using a flux compression scheme. This approach depends on the magnetic Reynolds number of the engine exhaust jet being greater than unity; however, this may actually be achievable through geometrical focusing of the detonation wave. The authors have previously been examining various flux compression reactor concepts,[12,13] and are inclined to adapt some of these approaches to experimentally investigate this idea. For example, a pulsed 2-T solenoid magnet was recently developed, tested, and delivered to MSFC for general research use,[14] and the authors are currently evaluating the use of this magnet as the basis for a pulse detonation-driven flux compression reactor experiment.

6. CONCLUSIONS

An experimental OH-fired, CsOH-seeded pulse detonation research engine (MSFC model PDRE–G–2) has been developed for the purpose of examining integrated propulsion and MHD power generation applications. The engine is based on a rectangular cross-section tube coupled to a converging-diverging nozzle, which is in turn attached to a segmented Faraday channel inserted in a 0.6-T permanent magnet assembly.

Initial experiments verified proper operation of the detonation driver, with and without the nozzle attachment, and tube-head pressure and time-resolved installed thrust measurements were acquired for both cases. The measured tube-head pressure profile for the nozzleless case was very similar to the ideal profile. For the nozzled engine, the pressure oscillated several cycles between the nozzle entrance and the tube head. As a result, the total impulse for the nozzled case was noticeably less than that without the nozzle.

Optical emission spectra were acquired at the nozzle exit plane. The only prominent features in this spectra were numerous atomic transition lines for Cs, the OH(A–X) band head at 306 nm, and the sodium D lines. An effort was made to fit the OH band head at 306 nm to a synthetic spectra generated by the NEQAIR radiation code, but the fidelity of the data was too poor to make any conclusive estimate for temperature.

A polychromatic quadrature microwave interferometer was also used to interrogate the engine exhaust at the nozzle exit plane. This yielded an electron number density on the order of 10^{12} cm^{-3}. An anomalous attenuation of the signal was also observed during passage of the detonation wave front. The cause of this unanticipated effect remains unresolved.

MHD testing was carried out with a 24-electrode Faraday channel attached to the nozzle. The internal channel flow passage was 2.54 cm square, and the entire channel was placed inside a 0.6-T permanent magnetic assembly. Generator terminal voltages were acquired for various load impedances, and it was possible to deduce that the peak effective velocity was between 1,400 and 1,500 m/s. Unfortunately, the limited size of the channel and the low magnetic field caused the internal resistance of the generator to be dominated by the near electrode voltage drop. Increased scaling, improved seeding techniques, higher magnetic fields, and higher expansion ratios are expected to greatly improve performance, however. Therefore, it is recommended that future efforts be undertaken with increased area expansion ratios, larger channel bores, and much higher applied fields.

REFERENCES

1. Kailasanath, K.: "Recent Developments in the Research on Pulse Detonation Engines," AIAA Paper 2002–0470, American Institute of Aeronautics and Astronautics, January 2002.

2. Litchford, R.J.; Thompson, B.R.; and Lineberry, J.T.: "Pulse Detonation MHD Experiments," AIAA Paper 98–2918, American Institute of Aeronautics and Astronautics, June 1998.

3. Cambier, J.-L.: "MHD Power Extraction from a Pulse Detonation Engine," AIAA Paper 98–3876, American Institute of Aeronautics and Astronautics, July 1998.

4. Litchford, R.J.; Thompson, B.R.; and Lineberry, J.T.: "Towards Integrated Pulse Detonation Propulsion and MHD Power," AIAA Paper 99–3662, American Institute of Aeronautics and Astronautics, June 1999.

5. Litchford, R.J.; Thompson, B.R.; and Lineberry, J.T.: "Pulse Detonation MHD Power," *AIAA J. of Prop. Power*, Vol. 16, No. 2, pp. 251–262, 2000.

6. Litchford, R.J.: "Integrated Pulse Detonation Propulsion and Magnetohydrodynamic Power," NASA/TP—2001–210801, Marshall Space Flight Center, AL, January 2001.

7. Cambier, J.-L.: "MHD Power Generation from a Pulse Detonation Rocket Engine," AIAA Paper 2002–2115, American Institute of Aeronautics and Astronautics, May 2002.

8. Litchford, R.J.: "Development of a Gas-Fed Pulse Detonation Research Engine," AIAA Paper 2001–3814, American Institute of Aeronautics and Astronautics, July 2001; NASA/TP—2001–211412, Marshall Space Flight Center, AL, December 2001.

9. Whiting, E.E.; Park, C.; Liu, Y.; Arnold, J.O.; and Patterson, J.A.: *NEQAIR96, Nonequilibrium and Equilibrium Radiative Transport and Spectra Program: User's Manual*; NASA Reference Publication 1389, Ames Research Center, Moffet Field, CA, December 1996.

10. Dobson, C.C.; and Jones, J.E.: "Polychromatic Quadrature Microwave Interferometer," Internal NASA MSFC Memo, to be published, February 2002.

11. Heald, M.A.; and Wharton, C.B.: *Plasma Diagnostics With Microwaves*, John Wiley & Sons, New York, 1965.

12. Litchford, R.J.; Robertson, G.A.; Hawk, C.W.; Turner, M.W.; and Koelfgen, S.: "Magnetic Flux Compression Reactor Concepts for Spacecraft Propulsion and Power," NASA/TP—2001–210793, Marshall Space Flight Center, AL, 2001.

REFERENCES (Continued)

13. Turner, M.W.; Hawk, C.W.; and Litchford, R.J.: "Inductive Measurement of Plasma Jet Electrical Conductivity," NASA/TP—2001–210794, Marshall Space Flight Center, AL, 2001.

14. Goodrich, R.G.; Pullam, B.; Rickle, D.; Litchford, R.J.; Robertson, G.A.; and Schmidt, D.D.: "High-Purity Aluminum Magnet Technology for Advanced Space Transportation Systems," NASA/TP—2002–211464, Marshall Space Flight Center, AL, 2002.

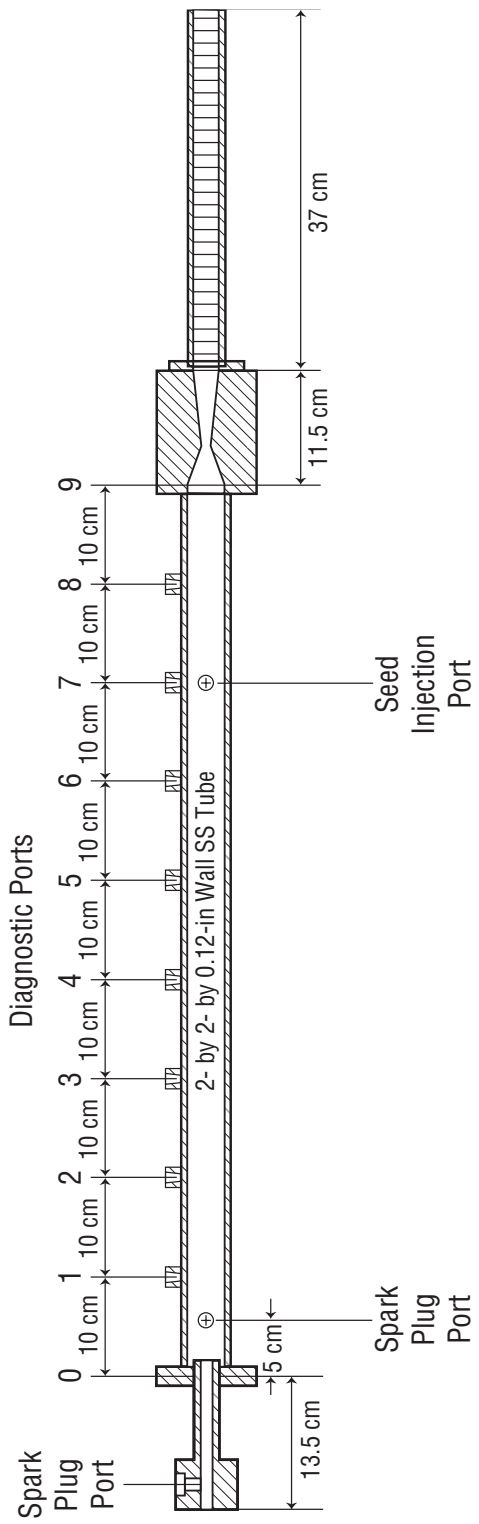

Figure 1. Schematic of the NASA MSFC PDRE–G–2 research engine. The major flow path components are: (1) Integrated injector/initiator assembly, (2) primary tube, (3) converging-diverging nozzle section, and (4) segmented Faraday channel (0.6-T permanent magnet assembly not shown). The system exhausts into the open atmosphere.

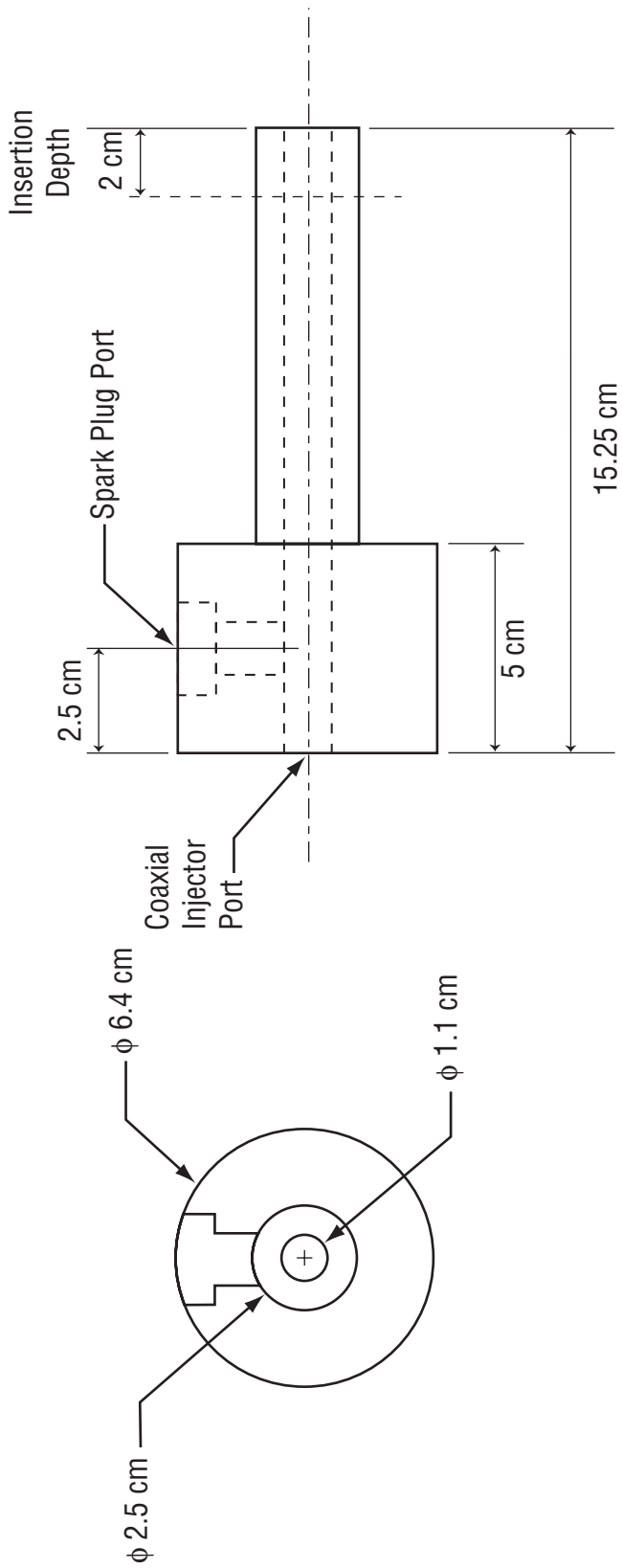

Figure 2. Cross-sectional drawing of the integrated injector/initiator assembly.

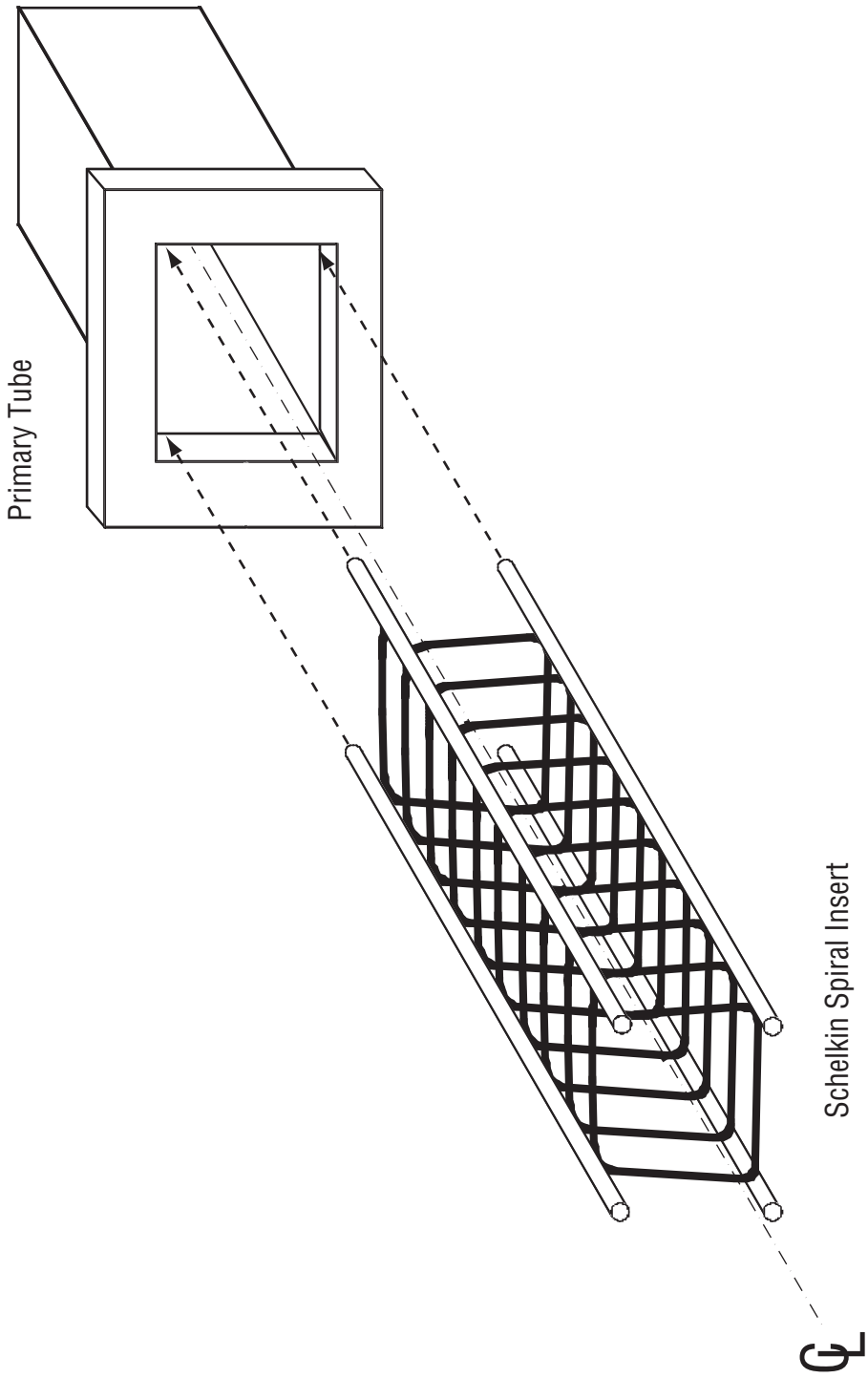

Figure 3. Schelkin spiral insert for primary detonation tube.

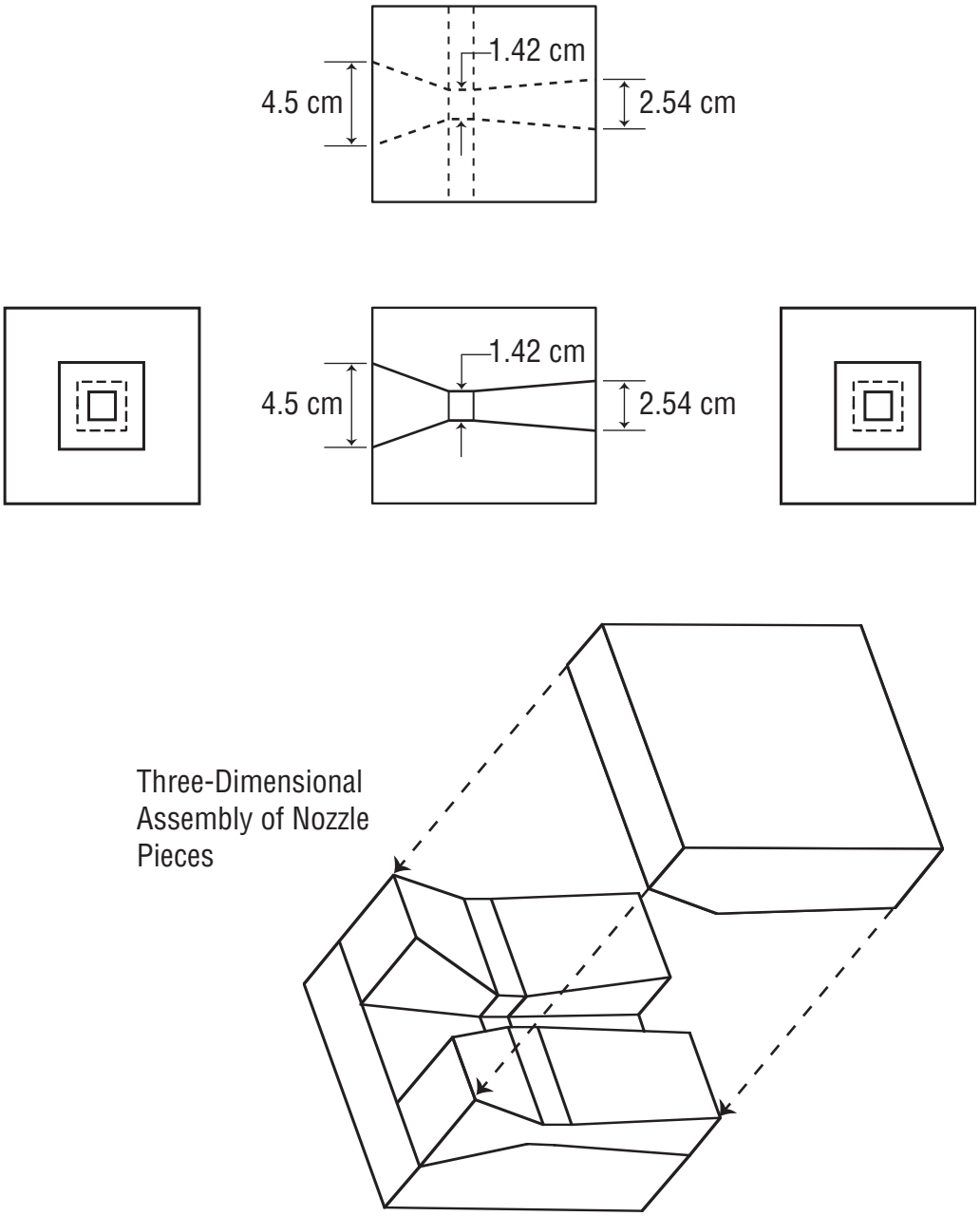

Figure 4. Schematic of aluminum nozzle assembly.

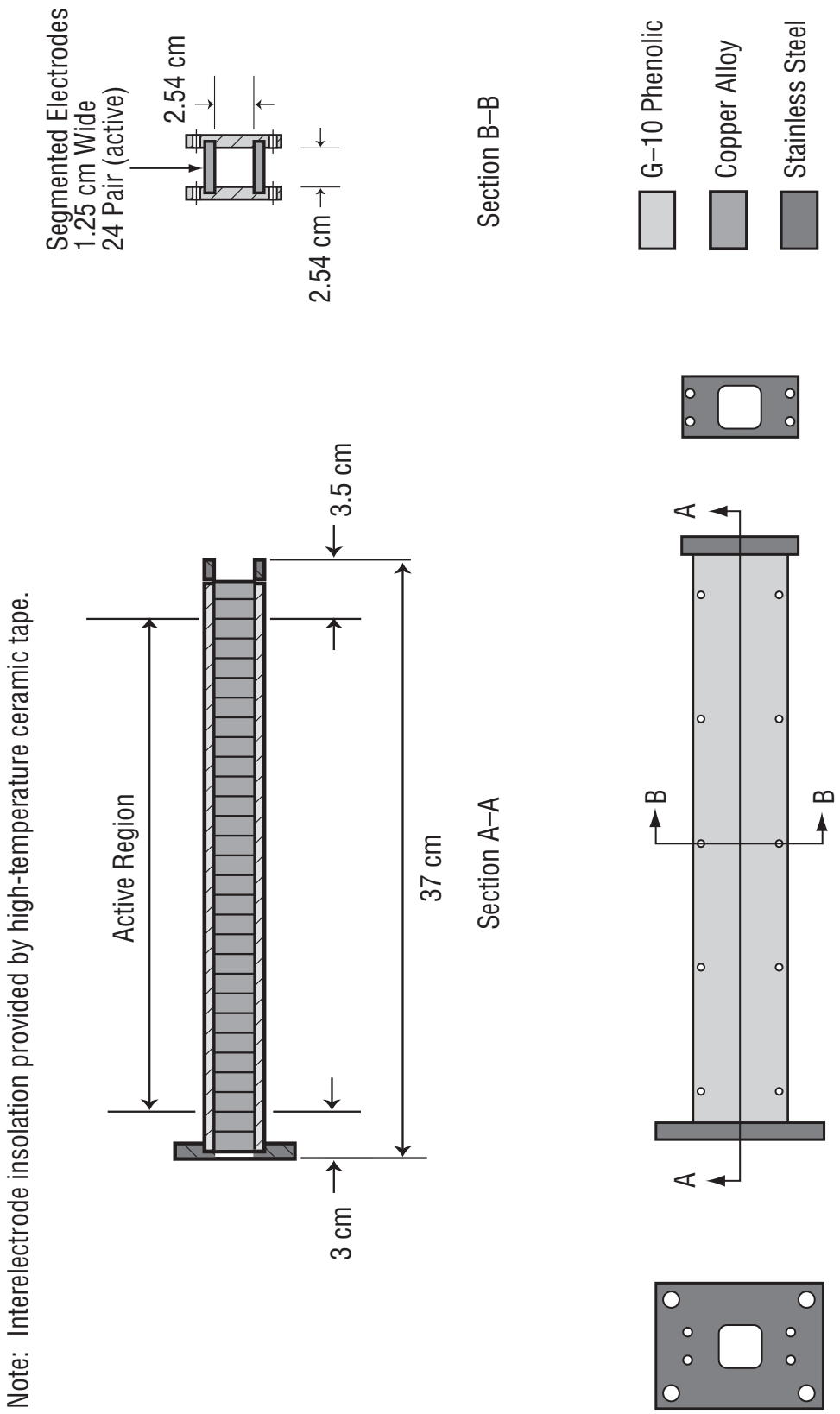

Figure 5. Exploded schematic of segmented Faraday channel with 24 active electrode pairs.

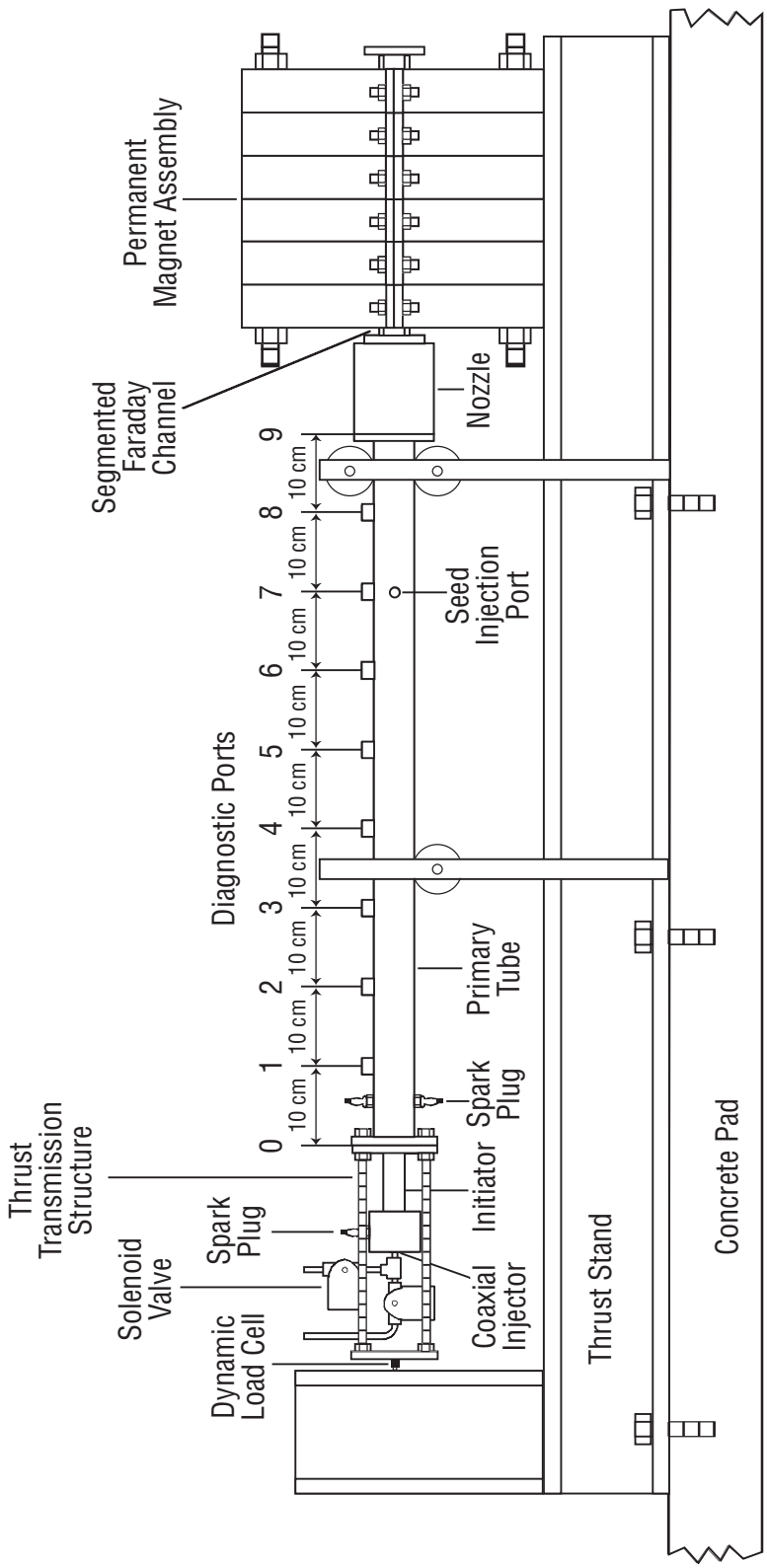

Figure 6. Schematic of fully assembled PDRE–G–2 research engine on the thrust stand with nozzle and MHD generator attached.

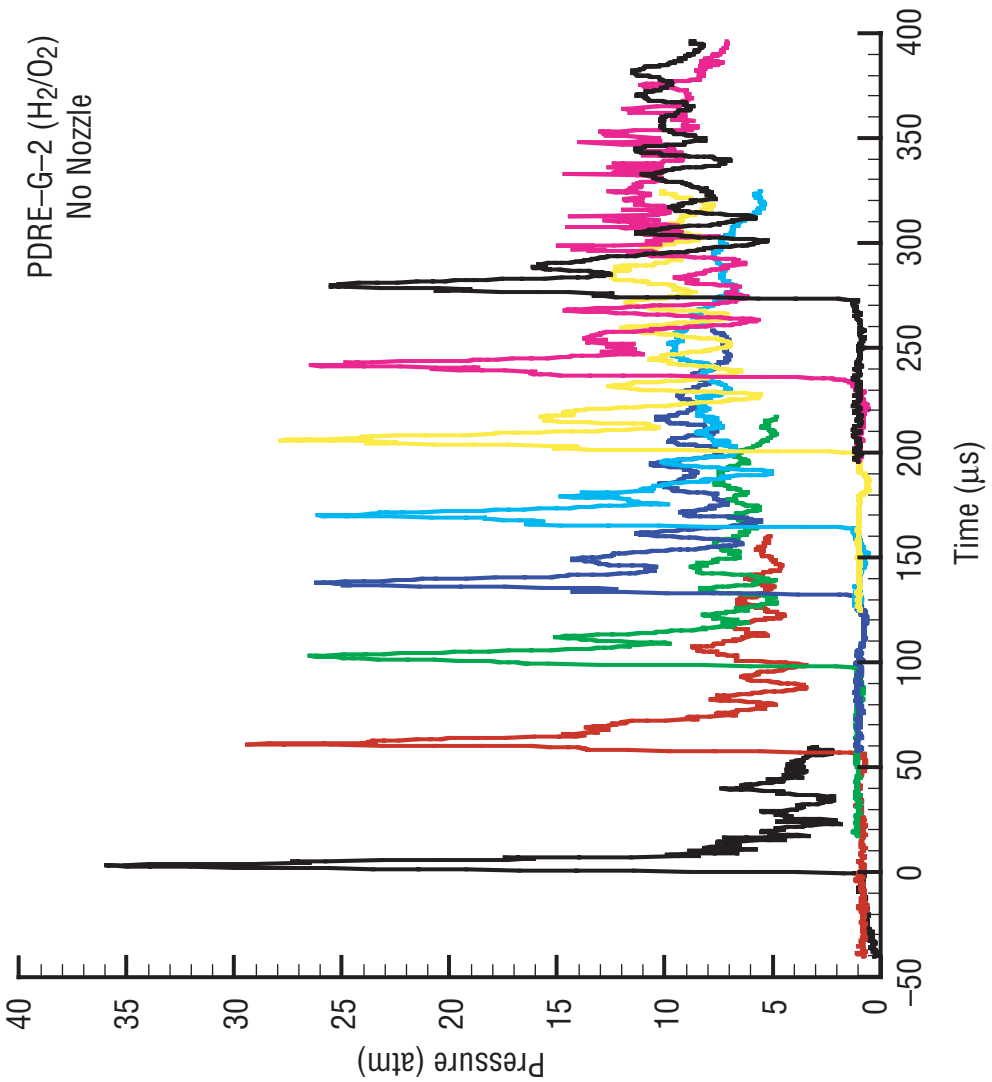

Figure 7. Axial pressure profiles without nozzle as measured at ports 1 through 8.

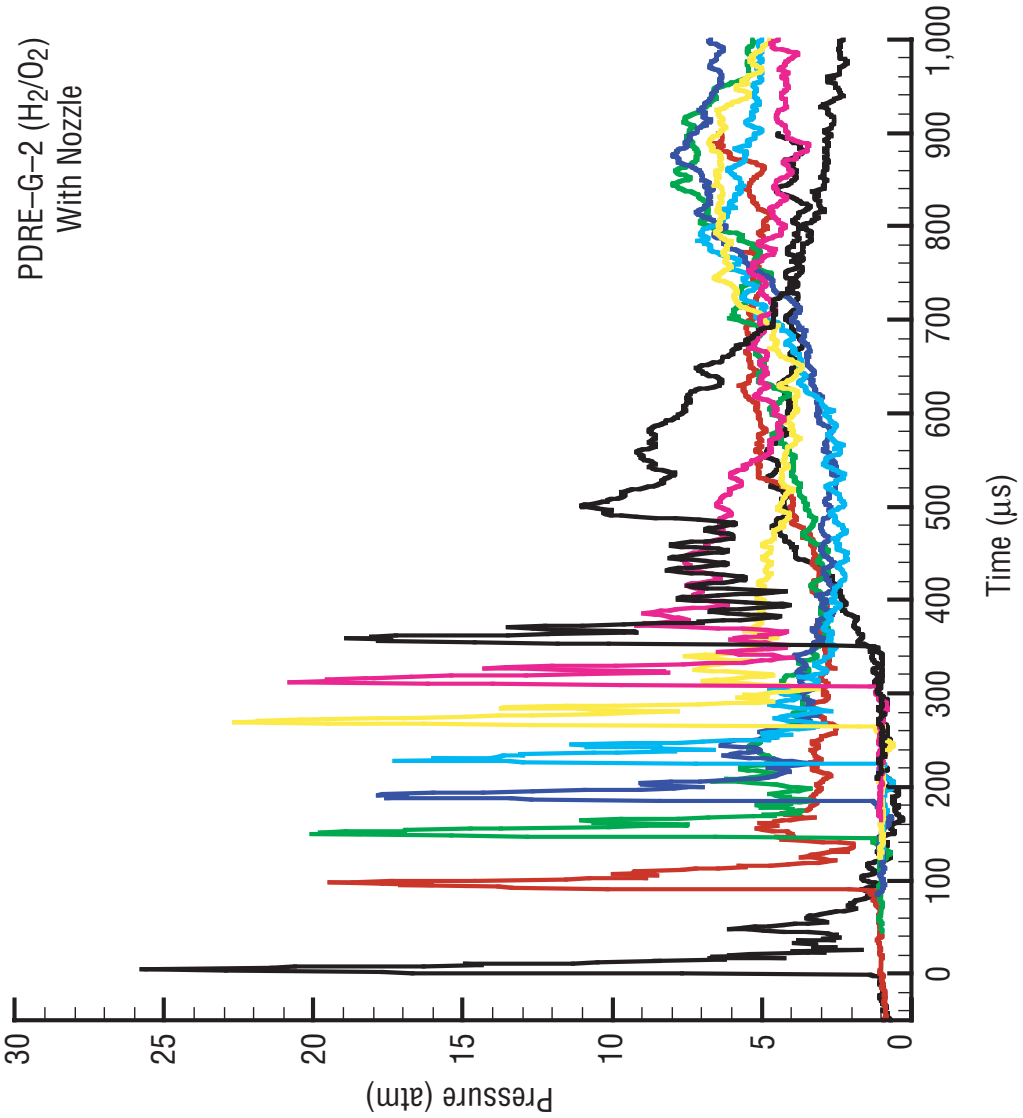

Figure 8. Axial pressure profiles with nozzle as measured at ports 1 through 8.

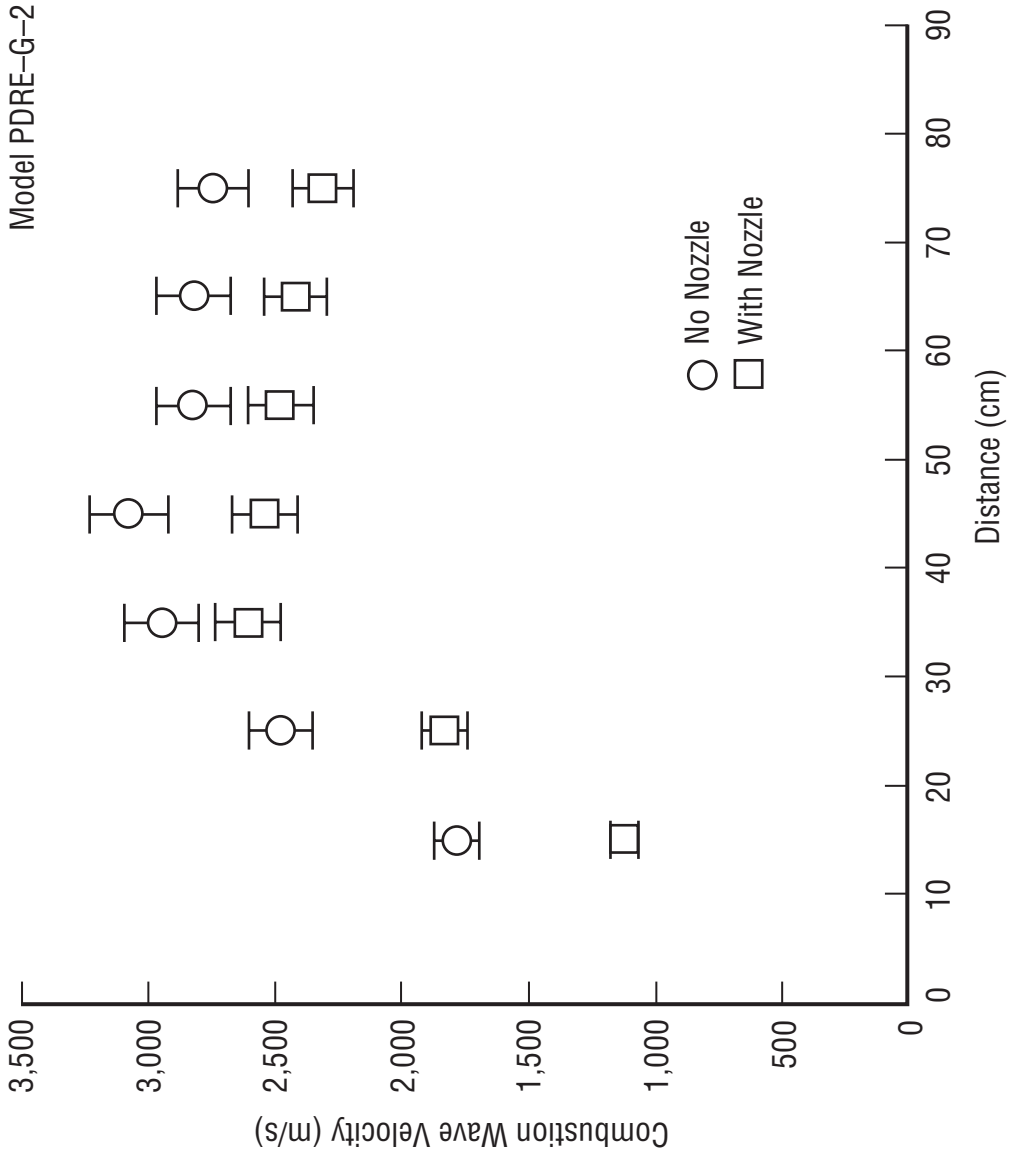

Figure 9. Combustion wave velocity distribution.

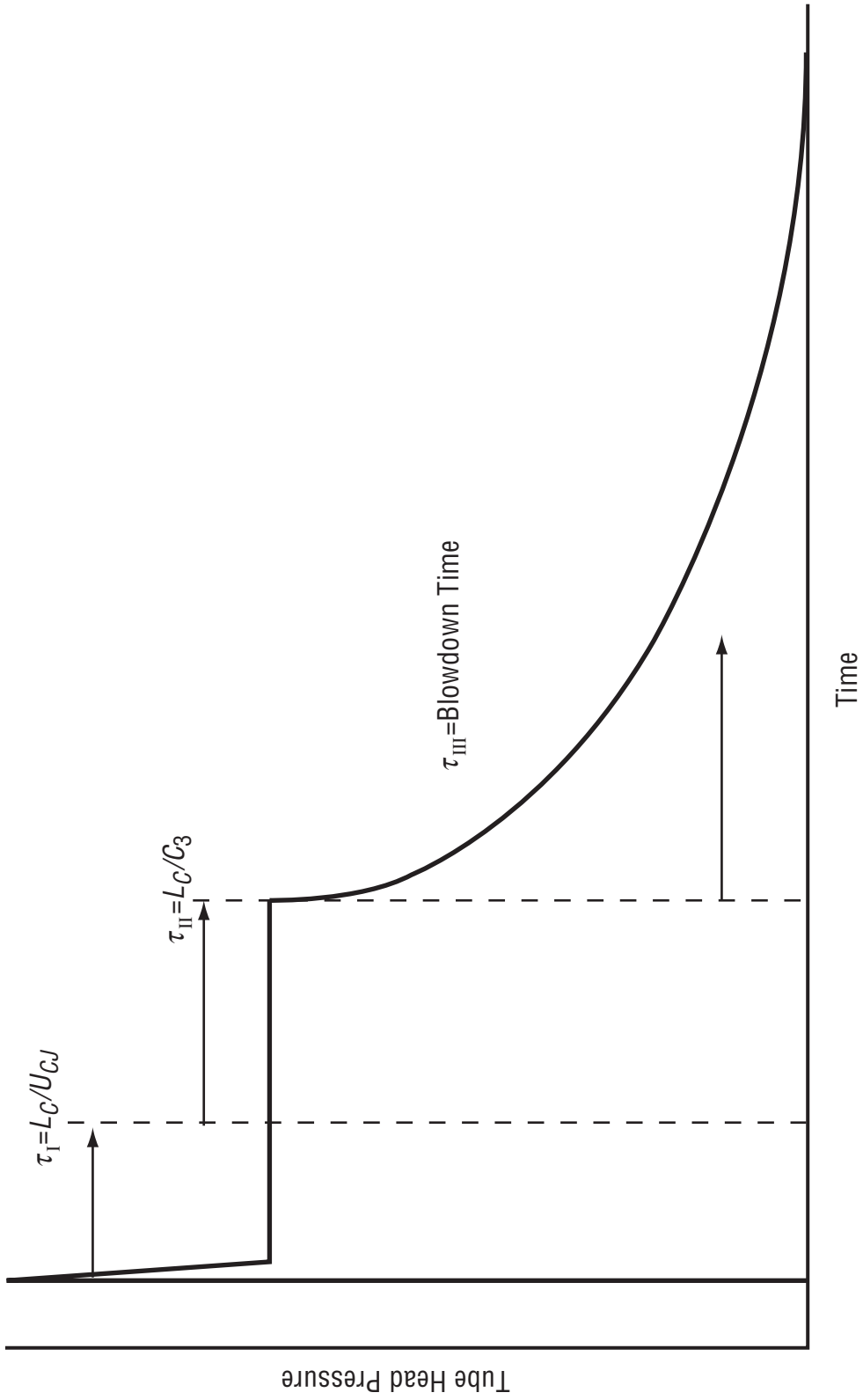

Figure 10. Ideal tube head pressure profile for a nozzleless straight-tube pulse detonation engine with head-end ignition.

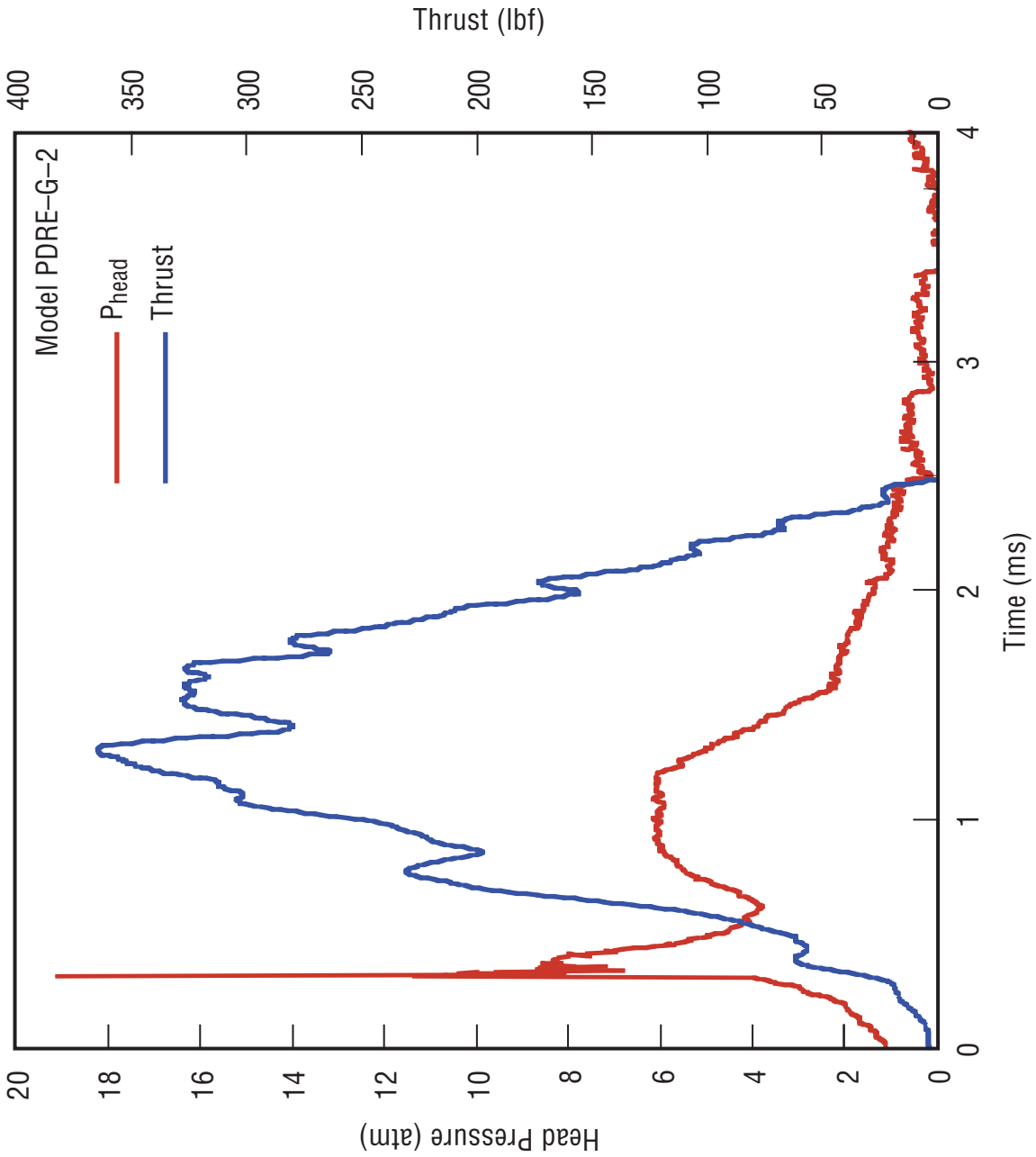

Figure 11. Time-resolved tube head pressure and installed thrust profiles without nozzle.

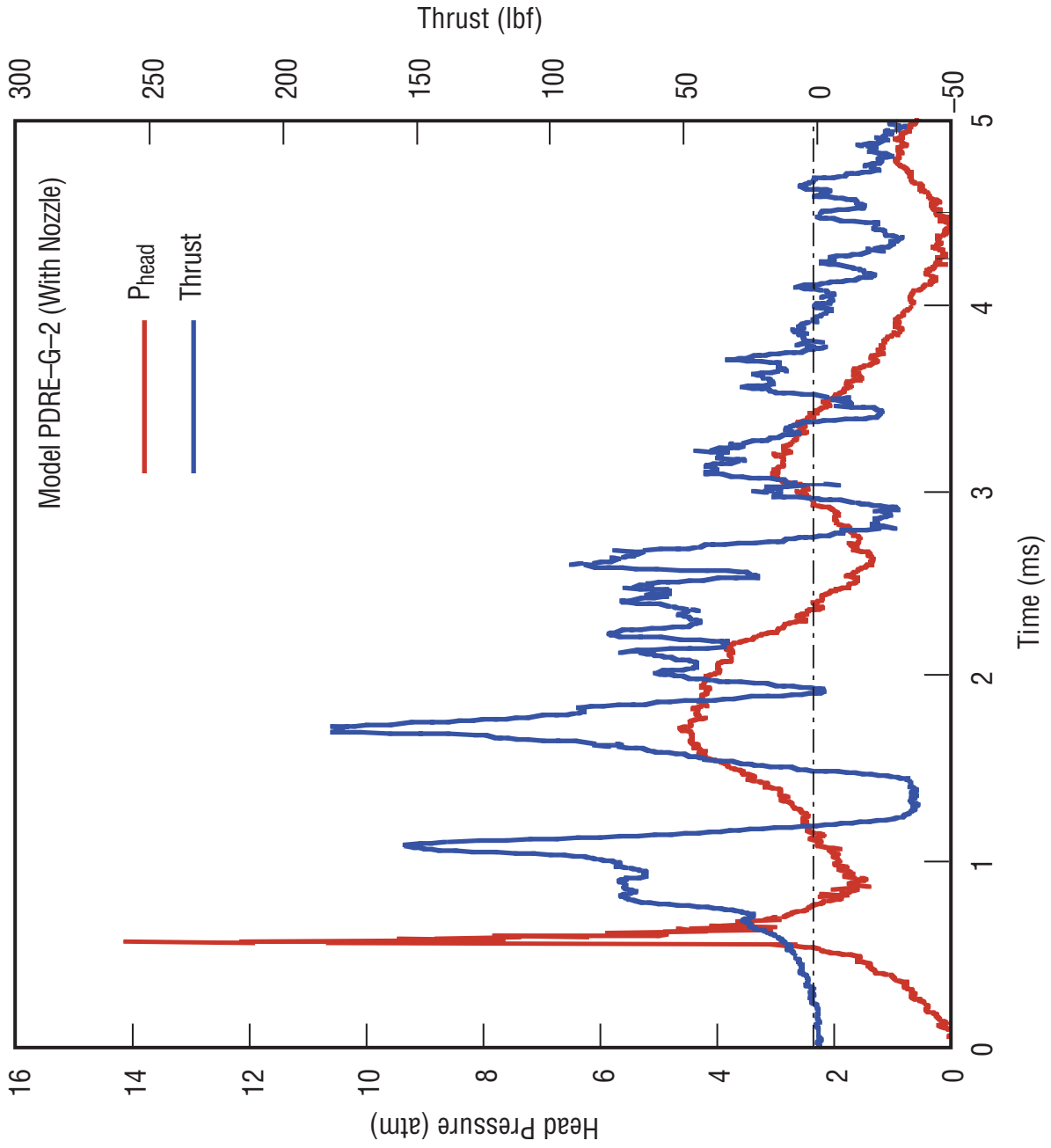

Figure 12. Time-resolved tube head pressure and installed thrust profiles with nozzle.

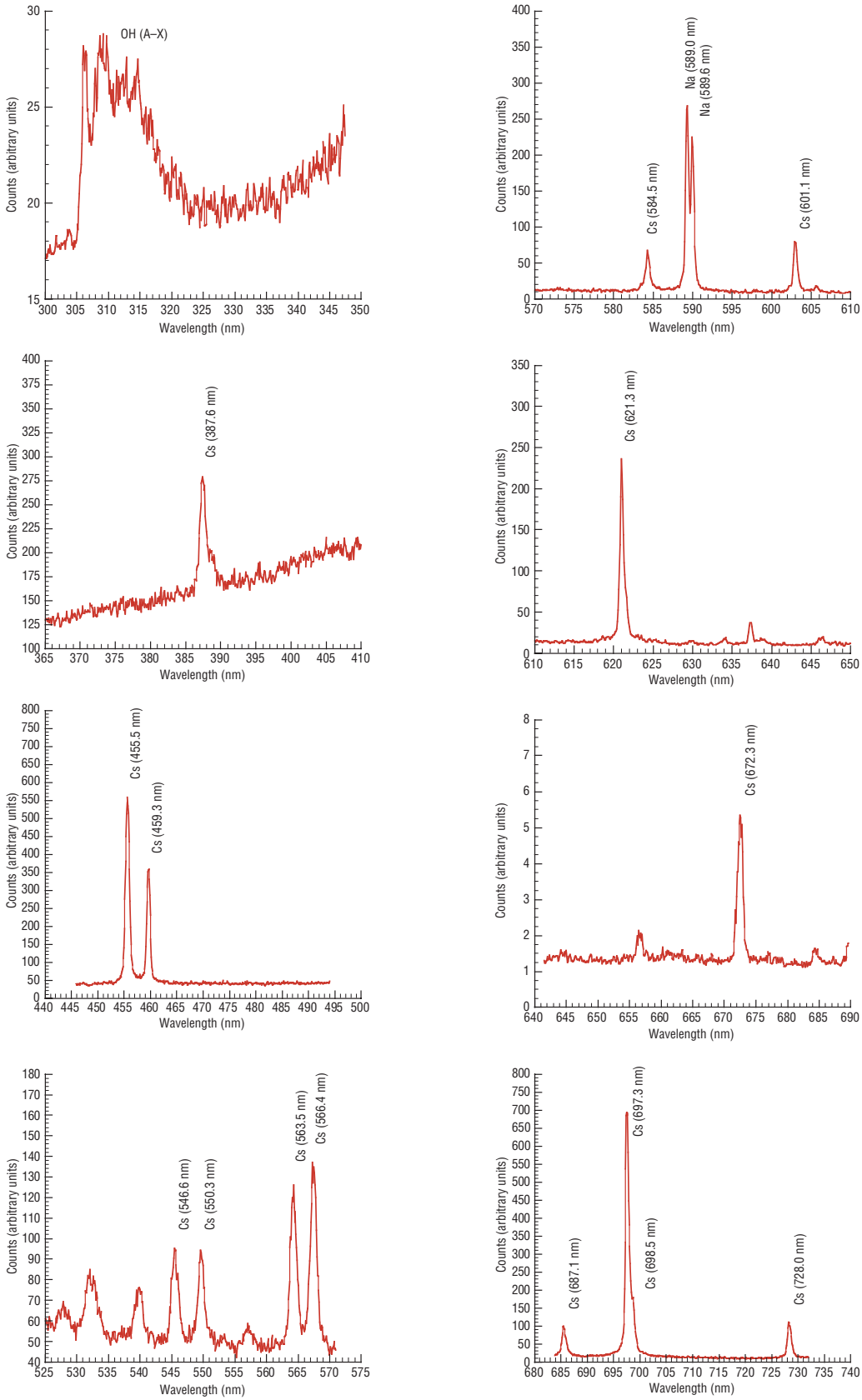

Figure 13. Summary of emission spectroscopy survey at engine nozzle exit.

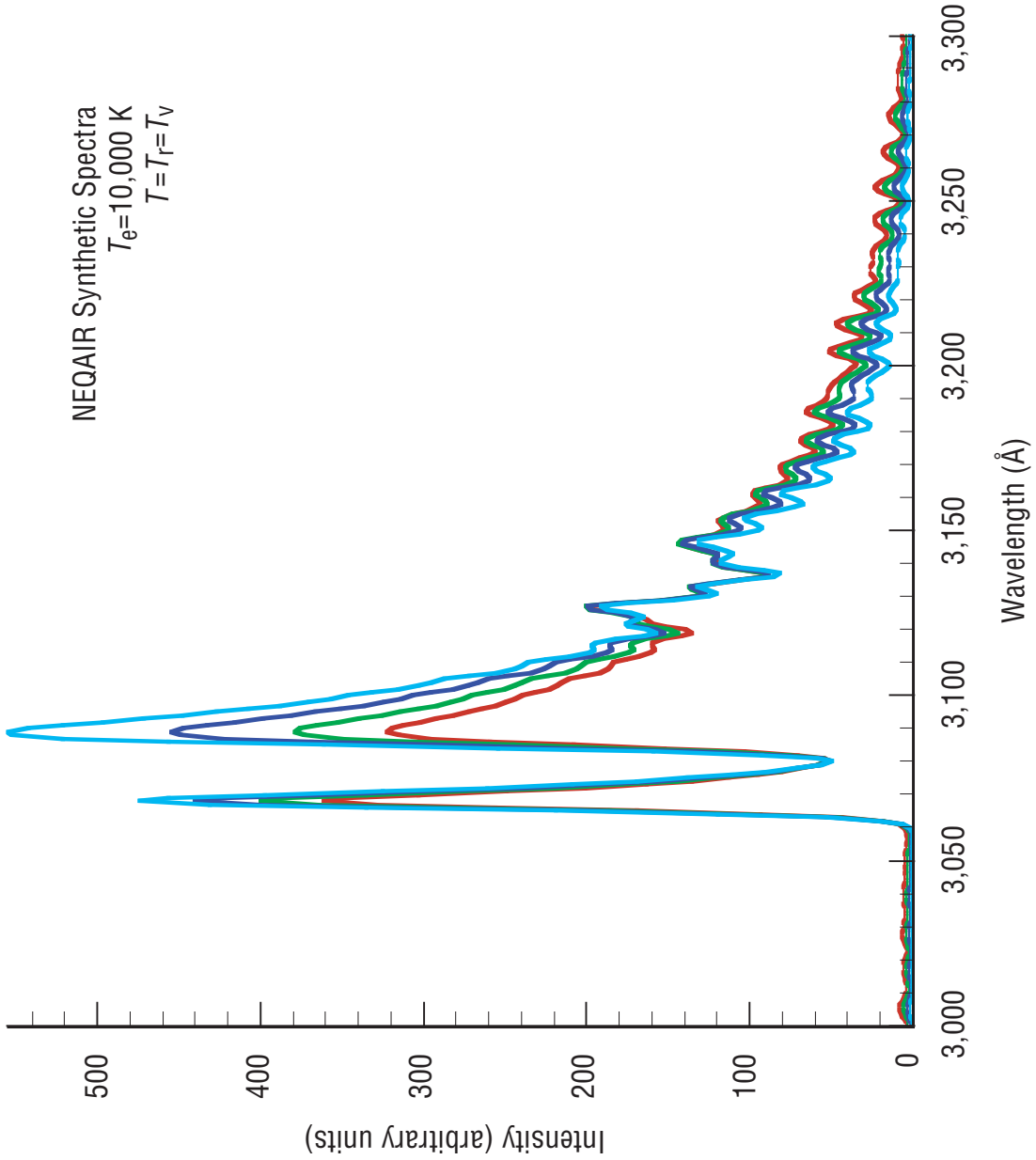

Figure 14. Synthetic spectra of the OH band head at 306 nm as generated by the NASA NEQAIR radiation code for equilibrium temperatures of 4,000, 3,500, 3,000, and 2,500 K. Assumes an electronic temperature of 10,000 K.

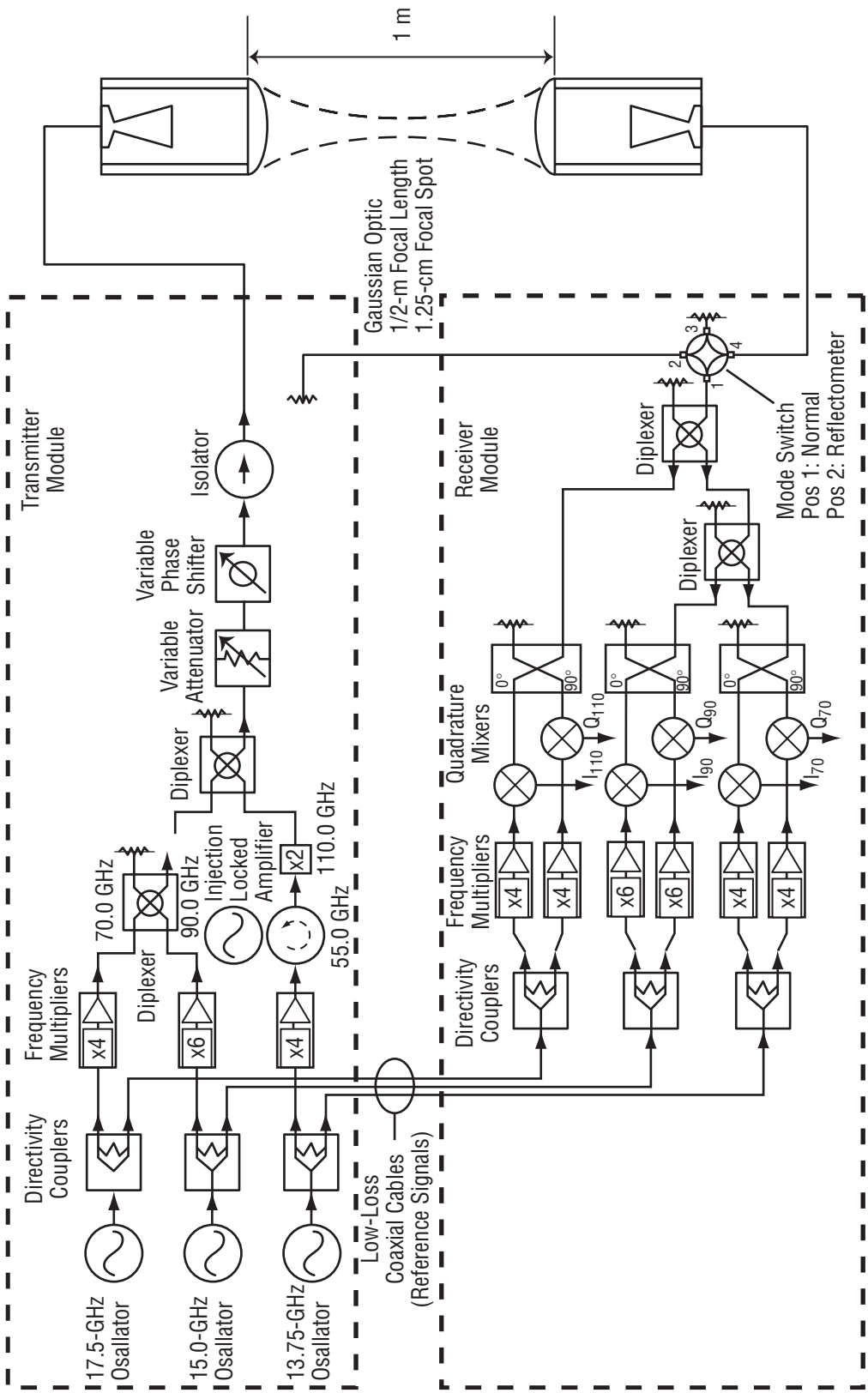

Figure 15. Schematic of polychromatic quadrature microwave interferometer.

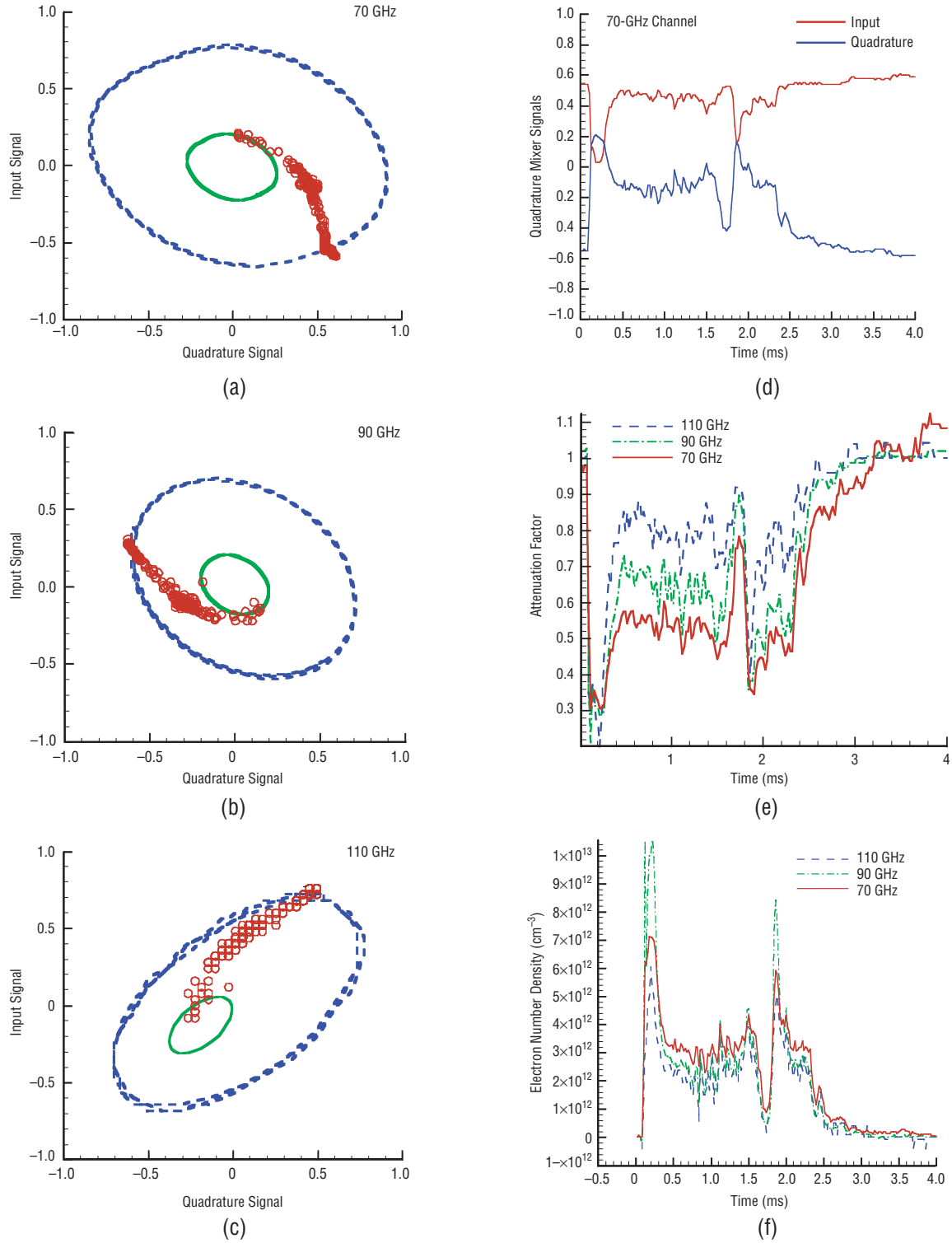

Figure 16. Summary of microwave interferometer interrogation of the PDRE–G–2 engine exhaust at the nozzle exit plane: (a) 70-GHz calibration, attenuated calibration, and data; (b) 90-GHz calibration, attenuated calibration, and data; (c) 110-GHz calibration, attenuated calibration, and data; (d) raw signal from 70-GHz channel; (e) attenuation factor for all three channels; and (f) electron number density as measured for all three interrogation frequencies.

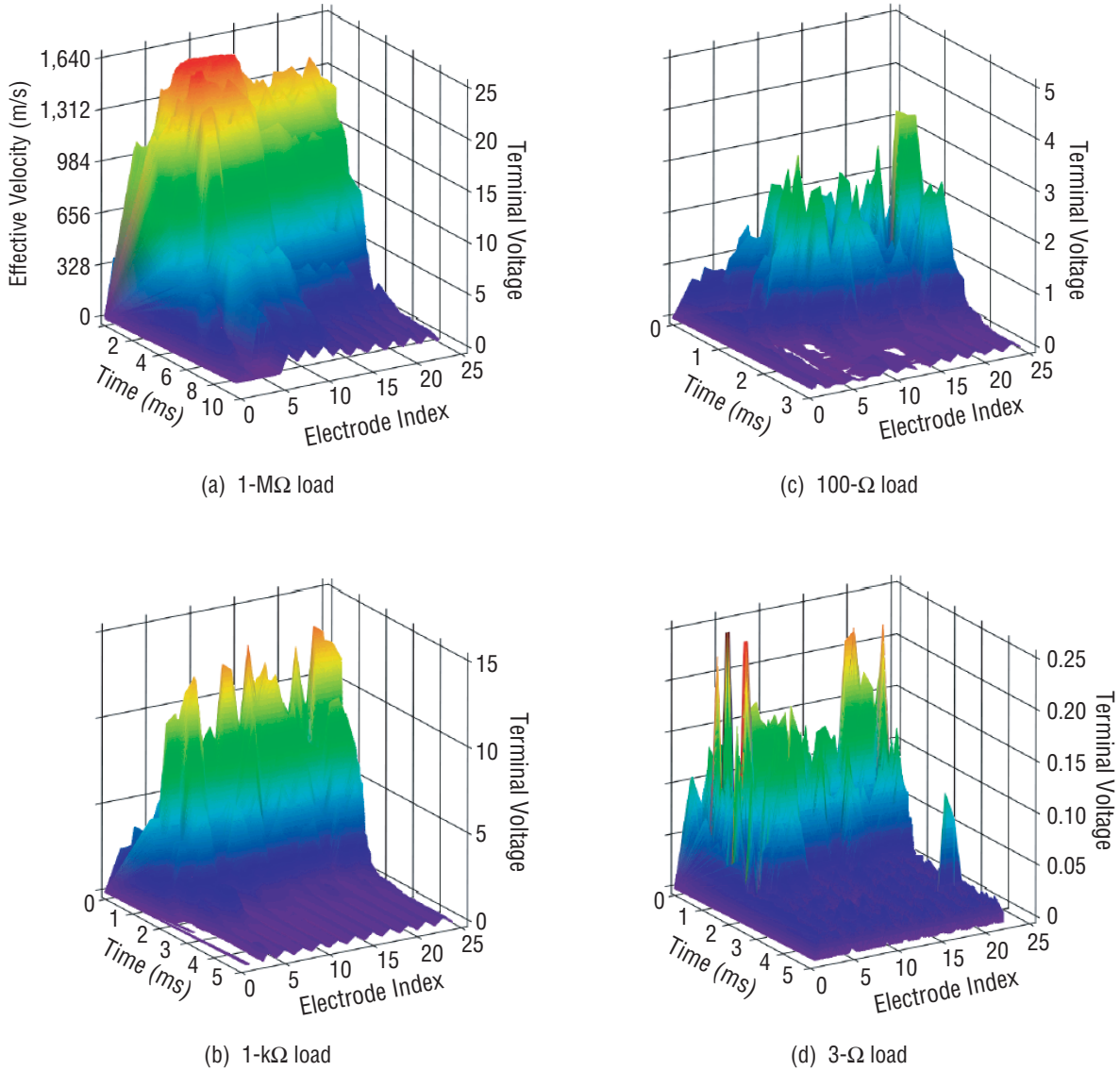

Figure 17. Summary of MHD testing using the PDRE–G–2 research engine: (a) 1-MΩ load and implied effective velocity, (b) 1-kΩ load, (c) 100-Ω load, and (d) 3-Ω load.

REPORT DOCUMENTATION PAGE

Form Approved
OMB No. 0704-0188

Public reporting burden for this collection of information is estimated to average 1 hour per response, including the time for reviewing instructions, searching existing data sources, gathering and maintaining the data needed, and completing and reviewing the collection of information. Send comments regarding this burden estimate or any other aspect of this collection of information, including suggestions for reducing this burden, to Washington Headquarters Services, Directorate for Information Operation and Reports, 1215 Jefferson Davis Highway, Suite 1204, Arlington, VA 22202-4302, and to the Office of Management and Budget, Paperwork Reduction Project (0704-0188), Washington, DC 20503

1. AGENCY USE ONLY *(Leave Blank)*

2. REPORT DATE
February 2003

3. REPORT TYPE AND DATES COVERED
Technical Publication

4. TITLE AND SUBTITLE
Pulse Detonation Rocket Magnetohydrodynamic Power Experiment

5. FUNDING NUMBERS

6. AUTHORS
R.J. Litchford, J.E. Jones, C.C. Dobson, J.W. Cole, B.R. Thompson,*
D.H. Plemmons,** and M.W. Turner***

7. PERFORMING ORGANIZATION NAMES(S) AND ADDRESS(ES)
George C. Marshall Space Flight Center
Marshall Space Flight Center, AL 35812

8. PERFORMING ORGANIZATION REPORT NUMBER
M–1063

9. SPONSORING/MONITORING AGENCY NAME(S) AND ADDRESS(ES)
National Aeronautics and Space Flight Center
Washington, DC 20546–0001

10. SPONSORING/MONITORING AGENCY REPORT NUMBER
NASA/TP—2003–212284

11. SUPPLEMENTARY NOTES
*TMET, Winchester, TN; **Plemmons Consulting, Lynchburg, TN;
***The University of Alabama in Huntsville, Huntsville, AL
Prepared by The Advanced Space Transportation Program, Space Transportation Directorate

12a. DISTRIBUTION/AVAILABILITY STATEMENT
Unclassified-Unlimited
Subject Category 20
Standard Distribution

12b. DISTRIBUTION CODE

13. ABSTRACT *(Maximum 200 words)*

The production of onboard electrical power by pulse detonation engines is problematic in that they generate no shaft power; however, pulse detonation-driven magnetohydrodynamic (MHD) electrical power generation represents one intriguing possibility for attaining self-sustained engine operation and generating large quantities of burst power for onboard electrical systems. To examine this possibility further, a simple heat-sink apparatus was developed for experimentally investigating pulse detonation-driven MHD generator concepts. The hydrogen-oxygen-fired driver was a 90-cm-long stainless steel tube having a 4.5-cm square internal cross section and a short Schelkin spiral near the head-end to promote rapid formation of a detonation wave. The tube was intermittently filled to atmospheric pressure and seeded with a CsOH/methanol spray prior to ignition by electrical spark. The driver exhausted through an aluminum nozzle having an area contraction ratio of A^*/A_c=1/10 and an area expansion ratio of A_e/A^*=3.2 (as limited by available magnet bore size). The nozzle exhausted through a 24-electrode segmented Faraday channel (30.5-cm active length), which was inserted into a 0.6-T permanent magnet assembly. Initial experiments verified proper drive operation with and without the nozzle attachment, and head-end pressure and time-resolved thrust measurements were acquired. The exhaust jet from the nozzle was interrogated using a polychromatic microwave interferometer yielding an electron number density on the order of 10^{12} cm^{-3} at the generator entrance. In this case, MHD power generation experiments suffered from severe near-electrode voltage drops and low MHD interaction; i.e., low flow velocity, due to an inherent physical constraint on expansion with the available magnet. Increased scaling, improved seeding techniques, higher magnetic fields, and higher expansion ratios are expected to greatly improve performance.

14. SUBJECT TERMS
pulse detonation, power, magnetohydrodynamics, propulsion

15. NUMBER OF PAGES
44

16. PRICE CODE

17. SECURITY CLASSIFICATION OF REPORT	18. SECURITY CLASSIFICATION OF THIS PAGE	19. SECURITY CLASSIFICATION OF ABSTRACT	20. LIMITATION OF ABSTRACT
Unclassified	Unclassified	Unclassified	Unlimited

National Aeronautics and
Space Administration
AD33
George C. Marshall Space Flight Center
Marshall Space Flight Center, Alabama
35812